Editors' Suggestion

Linearly polarized RABBIT beyond the dipole approximation

Yijie Liao,[1] Yongkun Chen,[1] Jan Marcus Dahlström,[2,*] Liang-Wen Pi,[3,†] Peixiang Lu,[1,4] and Yueming Zhou[1,5,‡]

[1]*School of Physics and Wuhan National Laboratory for Optoelectronics, Huazhong University of Science and Technology, Wuhan 430074, China*

[2]*Department of Physics, Lund University, Box 118, SE-221 00 Lund, Sweden*

[3]*Center for Attosecond Science and Technology, Xi'an Institute of Optics and Precision Mechanics of the Chinese Academy of Sciences, Xi'an 710119, China*

[4]*Optics Valley Laboratory, Hubei 430074, China*

[5]*Hubei Optical Fundamental Research Center, Wuhan 430074, China*

(Received 3 June 2024; accepted 29 July 2024; published 21 August 2024)

We theoretically investigate nondipole effects in the reconstruction of attosecond beating by interference of two-photon transitions (RABBIT) of helium using linearly polarized extreme ultraviolet and infrared fields. By scanning the time delay between the two fields, we observe modulations in sidebands (SBs) both for angular-integrated photoelectron yield and forward-backward asymmetry in photoelectron distribution along the light-propagation direction. The SB modulations of the forward-backward *asymmetry* reveal Wigner and continuum-continuum time delays of the electron wave packets ionized via *nondipole* paths, different from the conventional RABBIT where only the dipole paths are involved. Furthermore, the time delays extracted from the *forward-backward* asymmetry show an abrupt jump as a function of polar emission angle of photoelectrons, due to the competition among continuum partial waves in *nondipole* laser-assisted photoionization.

DOI: 10.1103/PhysRevA.110.023109

I. INTRODUCTION

The photoelectric effect is one of the most fundamental quantum processes, and it has been investigated by a variety of pump-probe spectroscopies [1–3] since the advent of attosecond extreme ultraviolet (XUV) pulses [4,5]. For instance, the reconstruction of attosecond beating by interference of two-photon transitions (RABBIT) technique is widely employed to monitor the electronic dynamics on its natural timescale [6–9], using an XUV attosecond pulse train (APT) and a weak infrared (IR) probe field [2,3]. By changing the relative time delay between the XUV and IR fields, the photoelectron yields of sidebands (SBs) located between the main peaks are periodically modulated due to the interference between the electron wave packets ionized via different two-photon paths [5,10,11]. From the modulations of the SB signals, the relative phase of the ionized electron wave packets can be retrieved, which encodes the information of the laser fields [5,12] and of the electronic motions in laser-matter interaction [3,13–16]. Once the phase of the laser fields is known, we can obtain the intrinsic time delay of the electron wave packets in two-photon above-threshold ionization [2,3]. In the absence of resonances [17], this photoionization time delay can be approximately separated into Wigner and continuum-continuum (CC) time delays, respectively, corresponding to the bound-continuum (BC) and CC transitions [2,3,18].

For photoionization processes in the low-photon-energy range below 100 eV, the dipole approximation (DA) is well-grounded because electrons are ejected from the target's orbital of significantly small scale compared with the long wavelength of the impinging radiation [19–21]. In the short-wavelength regime of soft and hard x-rays, the breakdown of the DA is observed as a forward-backward asymmetry along the light-propagation direction in the angular distribution of photoelectrons [20,22–26]. Particularly, the manifestation of nondipole effects is greatly enhanced near Cooper minima [27,28], the zeros of Fano profiles [29,30], and electric-quadrupole resonances [31,32], where the amplitudes of electric-dipole transitions become vanishingly small [20]. In strong-field ionization of the long-wavelength regime, the DA also breaks down because the electronic dynamics are significantly influenced by the magnetic field component of the laser fields for the photoelectrons with higher velocities [33–44]. Recently, the RABBIT measurements on helium atoms [45] revealed nondipole effects in two-photon above-threshold ionization of the long-wavelength regime [46–51]. At an IR intensity of 5.88×10^{13} W/cm^2, the electron wave packets ionized by the two adjacent XUV bursts are shifted by 15 pm in position due to the Lorentz force of the IR field, and thus the photoelectron momentum distribution is modified [45]. Moreover, by observing the forward-backward asymmetry of the photoelectron yields, a discrepancy of 15 ± 10 as is resolved between the photoionization time delays of electric-dipole and electric-quadrupole transitions [45].

In this work, we revisit the nondipole RABBIT measurements of a helium atom using linearly polarized XUV and *weak* IR fields. At low IR intensities, the strong-field

*Contact author: marcus.dahlstrom@matfys.lth.se
†Contact author: lwpi@opt.ac.cn
‡Contact author: zhouymhust@hust.edu.cn

effects from the magnetic components of the laser fields, e.g., the Lorentz force, are negligible, which enables us to isolate the perturbative influence of electric-quadrupole transitions on the photoionization time delay. By varying the time delay between the XUV and IR fields, the SB signals of the forward-backward asymmetry along the light-propagation direction are modulated with different phases, compared to the angular-integrated photoelectron yields [45]. In the nondipole RABBIT scheme, BC and CC transitions can be either electric-dipole or electric-quadrupole in two-photon above-threshold ionization.[1] According to selection rules, the dipole (nondipole) paths have isotropic (anisotropic) continuum partial waves over an azimuthal angle from the spherically symmetric $1s$ ground state of helium. Hence, the SB modulations in angular-integrated photoelectron spectra only imprint the photoionization time delays of the electronic wave packets ionized through dipole paths. However, in the forward-backward asymmetry of photoelectron spectra, the SB modulations result from the interference of the dipole paths with the nondipole paths, which encode the Wigner and CC time delays related to electric-quadrupole transitions. Moreover, we show that the time delays extracted from the forward-backward asymmetry exhibit sudden jumps as a function of the polar emission angle of photoelectrons, due to the competition among continuum partial waves in nondipole laser-assisted photoionization.

This paper is structured as follows. In Sec. II, we introduce the nondipole time-dependent Schrödinger equation (Sec. II A) and perturbation theory including nondipole effects (Sec. II B). In Sec. III, we analyze the numerical results, including the photoelectron spectra (Sec. III A) and the extracted time delays (Sec. III B). The Wigner and CC phases in nondipole two-photon above-threshold ionization (Sec. III C), and the propensity rules in nondipole laser-assisted photoionization (Sec. III D), are also analyzed. We finish with a summary in Sec. IV. The paper ends with several Appendixes. Appendix A provides the derivations of the Hamiltonian used in the nondipole time-dependent Schödinger equation. Appendix B gives the derivations of the nondipole laser-atom interaction term in "length gauge." Appendix C introduces the electric-dipole-magnetic-dipole paths and their modifications to observables. Appendix D derives the analytical CC phases of electric-quadrupole transitions in the continuum. Appendix E gives the approximated expression for the forward-backward asymmetry in the photoelectron spectra. Atomic units are used throughout this paper unless otherwise stated.

II. THEORY

A. Nondipole time-dependent Schrödinger equation

To uncover the electronic dynamics in photoionization, we solve the time-dependent Schrödinger equation (TDSE) for the helium atom. The TDSE within the single-active-electron approximation is written as

$$i\frac{\partial\Psi(\mathbf{r},t)}{\partial t}=H\Psi(\mathbf{r},t), \tag{1}$$

where the nonrelativistic Hamiltonian is written in its minimal-coupling form [52]

$$H=\tfrac{1}{2}[\mathbf{p}+\mathbf{A}(\mathbf{r},t)]^2+V(\mathbf{r})-\phi(\mathbf{r},t), \tag{2}$$

with the scalar potential $\phi(\mathbf{r},t)=0$. Here the canonical momentum operator and the position of the electron are $\mathbf{p}=-i\boldsymbol{\nabla}$ and $\mathbf{r}$, respectively. The one-electron effective potential of the helium atom is modeled as $V(\mathbf{r})=-[1+\exp(-2.1325r)]/r$ [53]. The vector potential of the external laser field $\mathbf{A}(\mathbf{r},t)=\mathbf{A}(\xi=t-\hat{k}\cdot\mathbf{r}/c)$ contains the full spatial dependence of the electromagnetic field, where the light-propagation direction of the laser field is $\hat{k}=\mathbf{e}_y$ in our calculation, and $c=1/\alpha\approx 137$ is the speed of light (α is the fine structure constant). Including nondipole effects to the first order in $1/c$, the Hamiltonian in Eq. (2) is transformed to (see Appendix A for details) [54–59]

$$\begin{aligned}H=&\frac{1}{2}\mathbf{p}^2+\mathbf{p}\cdot\mathbf{A}(t)+V(\mathbf{r})\\&+\frac{1}{c}(\hat{k}\cdot\mathbf{p})\left(\mathbf{p}\cdot\mathbf{A}(t)+\frac{1}{2}\mathbf{A}^2(t)\right)\\&-\frac{1}{c}(\hat{k}\cdot\mathbf{r})\mathbf{A}(t)\cdot\boldsymbol{\nabla}V(\mathbf{r}),\end{aligned} \tag{3}$$

where $\mathbf{A}(t)$ is the laser vector potential at the position of the nucleus, i.e., $\mathbf{A}(\xi=t)=\mathbf{A}(\mathbf{r}=0,t)$.

In our calculation, the linearly polarized laser field is described as

$$\mathbf{A}(t)=[A_{\mathrm{XUV}}(t)+A_{\mathrm{IR}}(t-\tau)]\hat{\epsilon}, \tag{4}$$

where $A_{\mathrm{XUV}}(t)$ and $A_{\mathrm{IR}}(t-\tau)$ are the vector potentials of the XUV and IR fields, respectively. The time delay between the two fields is τ, and the polarization of the electric field is $\hat{\epsilon}=\mathbf{e}_z$. The vector potential of the time-delayed IR field is expressed as

$$\mathbf{A}_{\mathrm{IR}}(t-\tau)=A_\omega\Lambda^{\mathrm{A}}_{\mathrm{IR}}(t;\tau)\sin[\omega(t-\tau)], \tag{5a}$$

with the envelope function

$$\Lambda^{\mathrm{A}}_{\mathrm{IR}}(t-\tau)=\exp\left[-2\ln 2\frac{(t-\tau)^2}{\tau^2_{\mathrm{IR}}}\right]. \tag{5b}$$

Here A_ω is the amplitude of the field. In our numerical simulations, the central frequency $\omega=1.55$ eV is used for the IR field, which corresponds to a period of $T=2\pi/\omega=2.69$ fs. The full width at half-maximum (FWHM) of the IR field is $\tau_{\mathrm{IR}}=11.24T=30.25$ fs in laser intensity. The vector potential of the XUV field is modeled as an attosecond pulse train [60]

$$A_{\mathrm{XUV}}(t)=\sum_{n=-5}^{5}A_\Omega\Lambda^{\mathrm{A,(n)}}_{\mathrm{APT}}\Lambda^{\mathrm{A,(n)}}_{\mathrm{XUV}}(t)\sin[\omega_{\mathrm{XUV}}(t-nT/2)], \tag{6a}$$

where the relative amplitude of the nth XUV pulse in the pulse train is

$$\Lambda^{\mathrm{A,(n)}}_{\mathrm{APT}}=\exp\left[-2\ln 2\frac{(nT/2)^2}{\tau^2_{\mathrm{APT}}}\right], \tag{6b}$$

[1]The electric-dipole–magnetic-dipole paths are also allowed while they have small contributions.

and the envelope function of the nth XUV pulse is

$$\Lambda_{\mathrm{XUV}}^{\mathrm{A},(\mathrm{n})}(t) = (-1)^n \exp\left[-2\ln 2\frac{(t-nT/2)^2}{\tau_{\mathrm{XUV}}^2}\right]. \tag{6c}$$

Here A_Ω is the amplitude of the field. In our simulations, the central frequency $\omega_{\mathrm{XUV}} = 25\omega$ is used for the XUV field. The FWHM durations of the XUV attosecond pulses and the APT composed of 11 XUV bursts are $\tau_{\mathrm{XUV}} = 0.08T = 0.2153$ fs and $\tau_{\mathrm{APT}} = 1.5T = 4.0361$ fs in laser intensity, respectively.

The wave function of the TDSE is expanded as a partial wave series

$$\Psi(\mathbf{r},t) = \sum_{l=0}^{l_{\max}} \sum_{m=-l_{\max}}^{l_{\max}} Y_{l,m}(\theta,\varphi)\frac{R_{l,m}(r,t)}{r}, \tag{7}$$

where $Y_{l,m}(\theta,\varphi)$ are spherical harmonics with polar angle θ and azimuthal angle φ, and $R_{l,m}(r,t)$ is the radial part of the wave function. The angular momentum quantum number and the magnetic quantum number are denoted as l and m, respectively. In our calculations, $R_{l,m}(r,t)$ is discretized by the finite-element discrete variable representation method [61], where the box size is $r_{\max} = 480.0$ a.u. The numerical convergence is reached with $l_{\max} = 5$. The initial state of the helium atom is obtained by imaginary-time propagation, yielding a binding energy of $I_{\mathrm{p}}^{1s} = 24.5978$ eV.

The time propagation of the wave function $\Psi(\mathbf{r},t)$ is implemented by the split-Lanczos method [62,63] with the time step $\Delta t = 0.01$ a.u. In each propagation step, the wave function $\Psi(\mathbf{r},t)$ is split into the inner part $\Psi_{\mathrm{in}}(\mathbf{r},t) = F(r)\Psi(\mathbf{r},t)$ and the outer part $\Psi_{\mathrm{out}}(\mathbf{r},t) = [1-F(r)]\Psi(\mathbf{r},t)$, using an absorbing mask function $F(r) = 1 - 1/[1+e^{(R_{\mathrm{c}}-r)/4.0}]$ with $R_{\mathrm{c}} = 200.0$ a.u. The inner part $\Psi_{\mathrm{in}}(\mathbf{r},t)$ is kept in the propagation governed by the full Hamiltonian H in Eq. (3), and the outer part $\Psi_{\mathrm{out}}(\mathbf{r},t)$ is approximately propagated by a Coulomb-Volkov propagator [64]. Specifically, the ionization amplitude of the photoelectrons with the momentum $\mathbf{p}$ at time t_i is obtained by projecting the outer part $\Psi_{\mathrm{out}}(\mathbf{r},t_i)$ on the scattering waves of helium [53] as

$$f(\mathbf{p},t_i) = \left\langle \psi_{\mathbf{p}}^{\mathrm{scat}}(\mathbf{r},t_i)\middle|\Psi_{\mathrm{out}}(\mathbf{r},t_i)\right\rangle. \tag{8a}$$

Then the total ionization amplitude at the final time t_f is expressed as

$$f(\mathbf{p}) = \sum_{i=1}^{N_{\mathrm{step}}} U_{\mathbf{p}}(t_i,t_f) f(\mathbf{p},t_i), \tag{8b}$$

where N_{step} is the number of propagation steps, and the time evolution factor,

$$U_{\mathbf{p}}(t_i,t_f) = \exp\left\{-i\int_{t_i}^{t_f}\left[\frac{\mathbf{p}^2}{2} + \mathbf{p}\cdot\mathbf{A}(t') + \frac{1}{c}(\hat{k}\cdot\mathbf{p})\left(\mathbf{p}\cdot\mathbf{A}(t') + \frac{\mathbf{A}^2(t')}{2}\right)\right]dt'\right\}, \tag{8c}$$

is expressed in terms of the Volkov phase with the nondipole correction [40,65,66]. Finally, the ionization probability distributions are obtained as

$$P(\mathbf{p}) = |f(\mathbf{p})|^2. \tag{8d}$$

B. Perturbation theory including nondipole effects

The Hamiltonian in Eq. (2) can be partitioned as $H = H_0 + H_{\mathrm{int}}$, where the atomic Hamiltonian is $H_0 = \mathbf{p}^2/2 + V(\mathbf{r})$ and the laser-atom interaction term H_{int} has the multipolar expansion under the Power-Zienau-Woolley transform in a Coulomb gauge [67–71]. Following Refs. [31,72–77], the effective interaction term for the field component j is given *to the first order in* $1/c$ as (see Appendix B for the alternative derivations in "length gauge")

$$H_{\mathrm{int,j}}^{(\pm)}(t) \approx E_j(t)\left(\hat{O}_{\mathrm{ED}} \pm \frac{ik_j}{2}\hat{O}_{\mathrm{EQ}}\right) + \frac{1}{2}B_j(t)\hat{O}_{\mathrm{MD}}, \tag{9}$$

where $E_j(t)$ and $B_j(t) = E_j(t)/c$ are the electric and magnetic fields of linear polarizations, respectively. The superscripts $(+)$ and $(-)$ denote the absorption and emission of photons, respectively. The operators for electric-dipole and electric-quadrupole transitions are $\hat{O}_{\mathrm{ED}} = (\hat{\epsilon}\cdot\mathbf{r}) = z$ and $\hat{O}_{\mathrm{EQ}} = (\hat{k}\cdot\mathbf{r})(\hat{\epsilon}\cdot\mathbf{r}) = yz$, respectively. Note that the electric-quadrupole transition has the scaling factor related to the photon momentum $k_j = \omega_j/c$, with $\omega_j > 0$ the photon frequency. The operator for the magnetic dipole transition is $\hat{O}_{\mathrm{MD}} = (\hat{k}\times\hat{\epsilon})\cdot\mathbf{L} = \mathbf{e}_x\cdot\mathbf{L} = L_x$, with L_x the x-component of the angular momentum operator $\mathbf{L} = \mathbf{r}\times\mathbf{p}$. The selection rules given by the electric-quadrupole transition operator $\hat{O}_{\mathrm{EQ}} = yz$ are $\Delta l = 0, \pm 2$ and $\Delta m = \pm 1$, and the selection rules given by the magnetic-dipole transition operator $\hat{O}_{\mathrm{MD}} = L_x$ are $\Delta l = 0$ and $\Delta m = \pm 1$. In principle, the two-photon paths with the magnetic-dipole transition followed by the electric-dipole transition are allowed (the electric-dipole-magnetic-dipole paths P_{EDMD}). However, due to their small contribution (see Appendix C for details), only the electric-dipole and electric-quadrupole terms are discussed in the following. In the RABBIT scheme, the ionization amplitudes are derived by the second-order time-dependent perturbation theory as [2,17,52,78]

$$\mathcal{A}_{f\leftarrow i}^{(2)} = -i\int_{-\infty}^{\infty} d\omega_1 \widetilde{E}_2(\omega_f-\omega_i-\omega_1)\widetilde{E}_1(\omega_1) \times \sum_{\nu}\frac{\langle\psi_f|\hat{O}|\psi_\nu\rangle\langle\psi_\nu|\hat{O}|\psi_i\rangle}{\omega_i+\omega_1-\omega_\nu+i0^+}, \tag{10}$$

where $|\psi_\beta\rangle$ denote the unperturbed states with the energy of ω_β, i.e., $H_0|\psi_\beta\rangle = \omega_\beta|\psi_\beta\rangle$, with $\beta = i, \nu, f$ corresponding to the initial, the intermediate, and the final states, respectively. The Fourier transform of the electric field is $\widetilde{E}_j(\omega_j) = (2\pi)^{-1/2}\int_{-\infty}^{\infty} E_j(t)e^{i\omega_j t}dt$ $(j = 1, 2)$. The total transition operator is $\hat{O} = \hat{O}_{\mathrm{ED}} \pm ik_j\hat{O}_{\mathrm{EQ}}/2$. Equation (10) describes the two-photon transition through the exchange of a photon ω_1 from the field $E_1(t)$ followed by exchanging a photon ω_2 from the field $E_2(t)$, either though electric-dipole or electric-quadrupole transitions, where the energy-preserving condition $\omega_f = \omega_i + \omega_1 + \omega_2$ is satisfied, with $\omega_{1,2} > 0$ $(\omega_{1,2} < 0)$ corresponding to absorption (emission). With the monochromatic approximation and separating the electric-dipole and electric-quadrupole contributions, the two-photon ionization has three

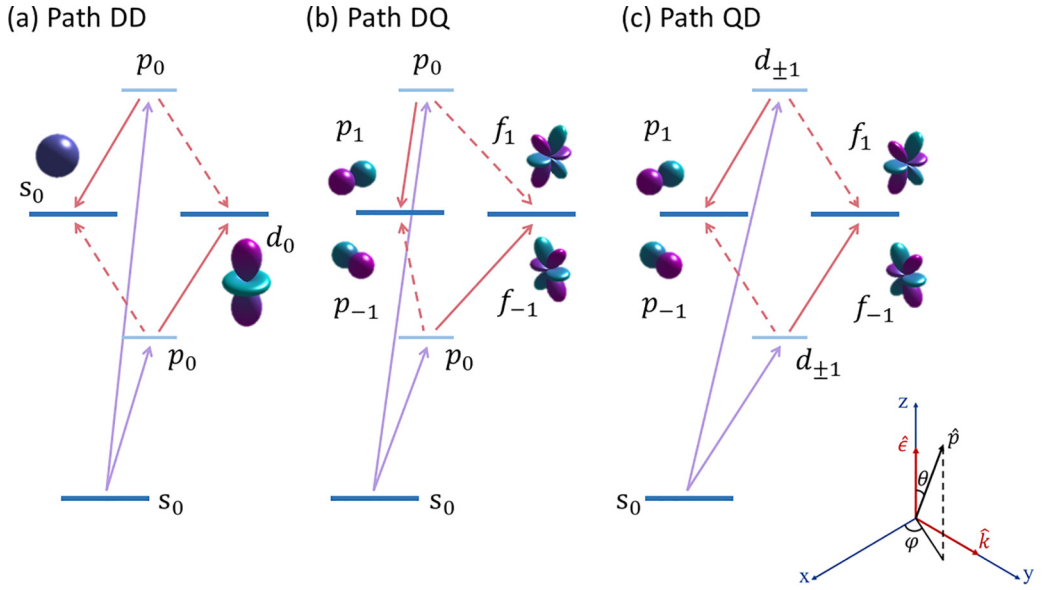

FIG. 1. The schematic of essential ionization channels in the nondipole RABBIT scheme for (a) dipole-dipole paths $P_{\rm DD}$, (b) dipole-quadrupole paths $P_{\rm DQ}$, and (c) quadrupole-dipole paths $P_{\rm QD}$. The purple and red arrows indicate the transitions by exchanging the XUV and IR photons, respectively. The upward (downward) arrows denote the absorption (emission) of a photon. The solid (dashed) arrows denote the relatively more (less) probable transition according to the propensity rule in laser-assisted photoionization when comparing each step of absorption and emission from the same state. The partial waves of each ionization channel are illustrated as the real spherical harmonics represented on polar plots. The inset depicts the coordinate system in our discussions, where $\hat{\epsilon}$, $\hat{k}$, and $\hat{p} = (\theta, \varphi)$, respectively, denote the directions for the polarization of the electric field, the light-propagation, and the emission of photoelectrons.

types of paths to the first order in $1/c$ [31,45,46],

$$\mathcal{A}_{\rm DD}^{(\pm)} = -\frac{i}{4} E_\omega E_\Omega e^{\pm i\omega\tau + i\phi_\Omega} \sum_v \frac{\langle\psi_f|\hat{O}_{\rm ED}|\psi_v\rangle\langle\psi_v|\hat{O}_{\rm ED}|\psi_i\rangle}{\omega_i + \Omega - \omega_v + i0^+},$$
$$\mathcal{A}_{\rm DQ}^{(\pm)} = \pm\frac{\omega}{8c} E_\omega E_\Omega e^{\pm i\omega\tau + i\phi_\Omega} \sum_v \frac{\langle\psi_f|\hat{O}_{\rm EQ}|\psi_v\rangle\langle\psi_v|\hat{O}_{\rm ED}|\psi_i\rangle}{\omega_i + \Omega - \omega_v + i0^+},$$
$$\mathcal{A}_{\rm QD}^{(\pm)} = \frac{\Omega}{8c} E_\omega E_\Omega e^{\pm i\omega\tau + i\phi_\Omega} \sum_v \frac{\langle\psi_f|\hat{O}_{\rm ED}|\psi_v\rangle\langle\psi_v|\hat{O}_{\rm EQ}|\psi_i\rangle}{\omega_i + \Omega - \omega_v + i0^+}, \tag{11}$$

where the amplitude of the IR electric field is E_ω, and the amplitude and the phase of the XUV harmonics are E_Ω and $\phi_\Omega = 0$, respectively. The superscripts $(+)$ and $(-)$ denote the absorption and emission of the IR photon after absorbing the XUV photon, respectively. For SB 2q at the photoelectron energy $\omega_f = 2q\omega - I_p^{1s}$, the frequency of the XUV photon is $\Omega = (2q-1)\omega$ [$\Omega = (2q+1)\omega$] in the absorption (emission) case. In Eqs. (11), the ionization amplitudes $\mathcal{A}_{\rm DD}^{(\pm)}$ correspond to the electric-dipole BC transition followed by the electric-dipole CC transition in two-photon above-threshold ionization (dipole-dipole paths $P_{\rm DD}$); the ionization amplitudes $\mathcal{A}_{\rm DQ}^{(\pm)}$ are related to the electric-dipole BC transition followed by the electric-quadrupole CC transition (dipole-quadrupole paths $P_{\rm DQ}$); and the ionization amplitudes $\mathcal{A}_{\rm QD}^{(\pm)}$ are associated with the electric-quadrupole BC transition followed by the electric-dipole CC transition (quadrupole-dipole paths $P_{\rm QD}$). The magnitudes of the nondipole paths $\mathcal{A}_{\rm DQ/QD}^{(\pm)}$ are roughly two orders less than the dipole paths $\mathcal{A}_{\rm DD}^{(\pm)}$, due to the existing factor $1/c$. We exclude the ionization paths with the two photons exchanged in a reversed time order due to their negligible contribution to the observables[2] focused on here [2,79].

Figure 1 shows the essential ionization channels in the nondipole RABBIT scheme, where the selection rules are $\Delta m = 0$ and $\Delta l = \pm 1$ ($\Delta m = \pm 1$ and $\Delta l = 0, \pm 2$) for electric-dipole (electric-quadrupole) transitions. In Fig. 1(a), the usual dipole RABBIT paths $P_{\rm DD}$ [18] have two ionization channels characterized by $s_0 \to p_0 \to \varepsilon s_0/\varepsilon d_0$ in both absorption and emission cases (here and hereafter the continuum partial wave is denoted as εl_m, with l the angular quantum number and m the magnetic quantum number). As shown in Fig. 1(b), the dipole-quadrupole paths $P_{\rm DQ}$ have four possible channels characterized by $s_0 \to p_0 \to \varepsilon p_{\pm1}/\varepsilon f_{\pm1}$ in both absorption and emission cases. Similarly, the quadrupole-dipole paths $P_{\rm QD}$ have four probable channels characterized by $s_0 \to d_{-1} \to \varepsilon p_{-1}/\varepsilon f_{-1}$ and $s_0 \to d_1 \to \varepsilon p_1/\varepsilon f_1$ for both absorption and emission of the IR photon, as given in Fig. 1(c). In all dipole and nondipole cases, the relative strength of the ionization channels in each path is determined by the propensity rule in laser-assisted photoionization [80,81]: the angular momenta of electrons are prone to increase (decrease) in absorbing (emitting) a photon in the continuum, as given in Fig. 1.

[2]As discussed in Sec. III, the focused observables are only relevant to the interference within the dipole paths, and to the interference of the dipole paths with the nondipole paths. In the absence of the resonances with bound states, the contributions of the dipole paths with the IR photon exchanged first can be safely neglected for both types of interferences.

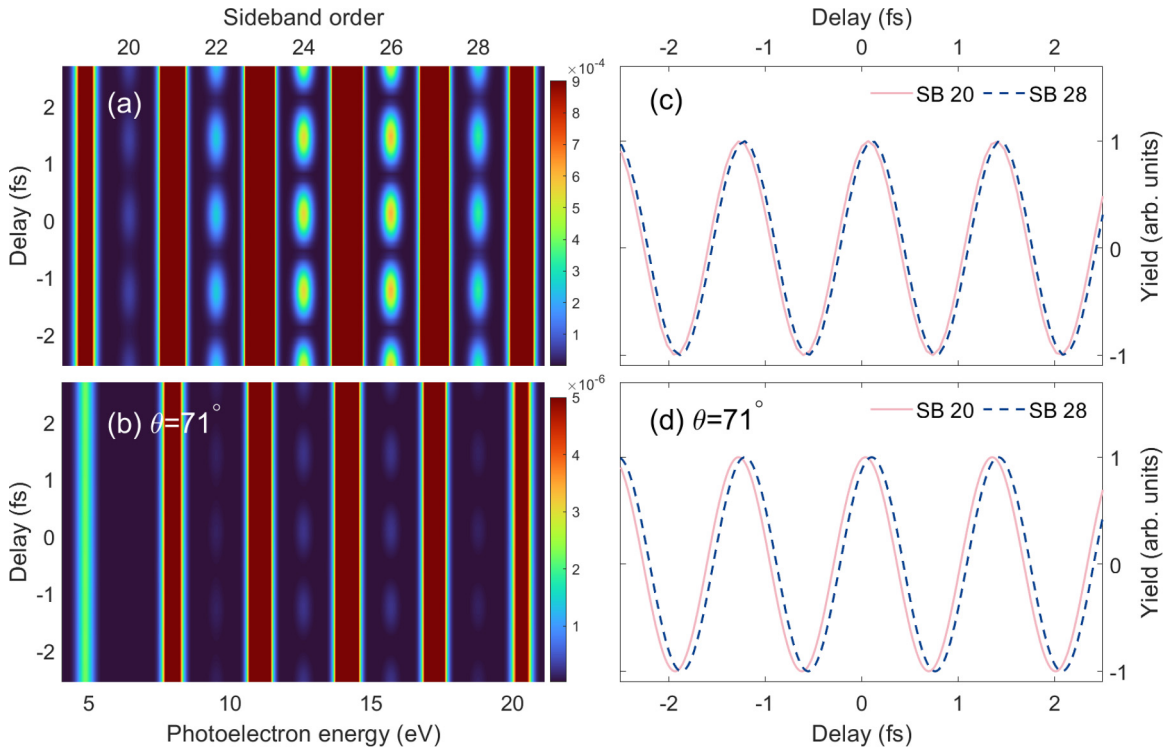

FIG. 2. (a) The angular-integrated photoelectron energy spectra obtained by solving the TDSE, as a function of time delay between the XUV and IR fields. The intensities of the XUV and IR fields are 1×10^{13} and 1×10^{10} W/cm^2, respectively. (b) The same as (a), but for the forward-backward asymmetry of the photoelectron spectra at polar emission angle $\theta = 71^\circ$ of photoelectrons. (c) The normalized $2\omega\tau$ oscillations of photoelectron yields for SB 20 and SB 28 of the angular-integrated photoelectron spectra. (d) The same as (c), but for the forward-backward asymmetry of the photoelectron spectra at polar emission angle $\theta = 71^\circ$. The solid and dashed lines correspond to SB 20 and SB 28, respectively.

In calculation, the incoming final continuum state $\psi_{\mathbf{p}}^{-}(\mathbf{r}) = \langle \mathbf{r}|\psi_f\rangle$ can be further expanded on the partial wave series as [82]

$$\psi_{\mathbf{p}}^{-}(\mathbf{r}) = \frac{1}{p^{1/2}} \sum_{l=0}^{\infty} \sum_{m=-l}^{l} i^l e^{-i\eta_l} Y_{l,m}^*(\hat{p}) R_{E,l}(r) Y_{l,m}(\hat{r}), \quad (12)$$

where the asymptotic momentum is $\mathbf{p} = p\hat{p}$ with $p = \sqrt{2E} = \sqrt{2\omega_f}$, and the emission direction of photoelectrons is $\hat{p} = (\theta, \varphi)$. The scattering phase $\eta_l = \sigma_l + \delta_l$ contains the Coulombic phase $\sigma_l = \arg[\Gamma(1 + l - iZ/p)]$ with the effective nuclear charge $Z = 1$, and the phase shift δ_l due to the short-range potential in the helium atom [53]. The energy-normalized radial wave function is $R_{El}(r)$ with its asymptotic behavior of $\sqrt{2/(\pi pr)}\sin[pr - l\pi/2 - Z\ln(2pr)/p + \sigma_l + \delta_l]$ when $r \to \infty$. Substituting Eq. (12) into Eqs. (11), the ionization amplitude of different paths can be written as

$$\mathcal{A}_{\mathcal{P}}^{(\pm)} = \frac{1}{p^{1/2}} \sum_{\mathcal{N}} e^{\pm i\omega\tau + i\phi_\Omega} \mathcal{M}_{\mathcal{P},\mathcal{N}}^{(\pm)} Y_{L,M}(\hat{p}). \quad (13)$$

Here $\mathcal{M}_{\mathcal{P},\mathcal{N}}^{(\pm)}$ is the reduced ionization amplitude of a specified ionization channel of the path $\mathcal{P} \in \{\mathrm{DD}, \mathrm{DQ}, \mathrm{QD}\}$, which is unambiguously characterized by the ensemble of the quantum numbers of the states throughout two-photon transitions, $\mathcal{N} = \{(l_i, m_i), (\lambda, \mu), (L, M)\}$. Here l_i, λ, and L (m_i, μ, and M), respectively, label the angular (magnetic) quantum numbers of the initial, the intermediate, and the final states. The amplitudes $\mathcal{M}_{\mathcal{P},\mathcal{N}}^{(\pm)}$ can be separated into the angular and radial integrals. Dealing with the infinite summation in the radial part by the Dalgarno-Lewis method [83], the radial part is calculated using the perturbed wave functions [84], which satisfy the inhomogeneous equation and the boundary conditions described in Ref. [85]. Particularly, the integration of two continuum wave functions appearing in Eqs. (11) is calculated by using a complex coordinate rotation method [86].

III. RESULTS

A. Photoelectron spectra

Figure 2(a) shows the usual RABBIT photoelectron energy spectra integrated over both polar and azimuthal emission angles of photoelectrons and as a function of the time delay between the XUV and IR fields, which are obtained by solving the TDSE within [78] and beyond the DA. Here the intensities of the XUV and IR fields are 1×10^{13} and 1×10^{10} W/cm^2, respectively. In the angular-integrated spectra, the photoelectron yields of SBs 20 to 28 are modulated at the frequency 2ω as a function of the time delay between the two fields, which imprints the relative phase of the electron wave packets ionized via the absorption and emission paths in Fig. 1. Figure 2(c) shows the normalized photoelectron yields of the 2ω oscillations in SB 20 and SB

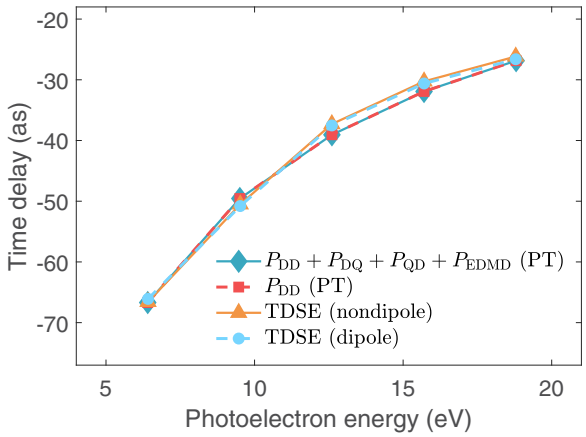

FIG. 3. The photoionization time delays extracted from the angular-integrated photoelectron spectra as a function of the photoelectron energy. The orange triangles and blue circles correspond to the results obtained by solving the TDSE beyond and within the DA, respectively. The red squares and green rhombuses refer to the PT results *excluding* and *including* the nondipole paths P_{DQ}, P_{QD}, and P_{EDMD} in addition to the dipole path P_{DD}, respectively.

28, which are obtained from the Fourier transform of the SB signals in Fig. 2(a). The $2\omega\tau$ oscillations of SB 20 are obviously retarded with respect to SB 28, which reveals the energy dependence of the phase of the outgoing electron wave packets.

Figure 2(b) shows the forward-backward asymmetry of the photoelectron yields at a polar emission angle $\theta = 71^\circ$. Here the forward-backward asymmetry is defined as the difference of the photoelectron yields between the parallel ($\varphi = \pi/2$) and antiparallel ($\varphi = 3\pi/2$) to the light-propagation direction (y-axis). The amplitudes of the asymmetry in Fig. 2(b) are two orders less ($\sim 1/c$) than the angular-integrated RABBIT photoelectron spectra in Fig. 2(a). Interestingly, the forward-backward asymmetry of the photoelectron yields in the SBs also displays 2ω modulations as a function of the time delay between the two laser fields. As shown in Fig. 2(d), the phases of $2\omega\tau$ oscillations also depend on the photoelectron energy, and they are obviously different from the angular-integrated SBs in Fig. 2(c).

B. Photoionization time delays

Figure 3 shows the photoionization time delays $\bar{t}_d$ from SB 20 to SB 28 as a function of the photoelectron energy, which are extracted by fitting the $2\omega\tau$ oscillations of the SB signals in angular-integrated photoelectron spectra with $S_{2q}^{2\omega} = B_0 \cos[2\omega(\tau - \bar{t}_d)]$. For the TDSE simulations in Fig. 2(a), the retrieved time delays are negative and they increase with the photoelectron energy. The TDSE results within and beyond the DA show an excellent agreement, which indicates that the angular-integrated time delays encode no nondipole effects. As a comparison, we use perturbation theory (PT) in Sec. II B to calculate the photoelectron yields of SBs 20 to 28 in angular-integrated photoelectron spectra as

$$\bar{\mathcal{I}}(E_{2q},\tau) = \int d\Omega \left| \sum_{\mathcal{P}'} (\mathcal{A}^{(+)}_{\mathcal{P}'}(E_{2q}) + \mathcal{A}^{(-)}_{\mathcal{P}'}(E_{2q})) \right|^2$$
$$= \frac{1}{p} \int d\Omega \left| \sum_{\mathcal{P}',\mathcal{N}} (e^{+i\omega\tau} \mathcal{M}^{(+)}_{\mathcal{P}',\mathcal{N}}(E_{2q}) Y_{L,M}(\hat{p}) + e^{-i\omega\tau} \mathcal{M}^{(-)}_{\mathcal{P}',\mathcal{N}}(E_{2q}) Y_{L,M}(\hat{p})) \right|^2, \quad (14)$$

with $E_{2q} = 2q\omega - I_p^{1s} = p^2/2$ the energy of SB 2q, and $\hat{p} = (\theta, \varphi)$ the emission direction of photoelectrons. Here we use the same laser parameters as the TDSE simulations, and the phases of XUV harmonics ϕ_Ω are zero. For comparison, we calculated the angular-integrated time delays by PT including [$\mathcal{P}' = \{DD, DQ, QD, EDMD\}$ in Eq. (14)] and excluding [$\mathcal{P}' = \{DD\}$ in Eq. (14)] the nondipole paths, which are also shown in Fig. 3. The PT results agree well with the TDSE results. The tiny discrepancy may be due to the monochromatic approximation of PT in Eqs. (11) and to the inadequate description of the CC transitions[3] by the Coulomb-Volkov propagator of TDSE in Eq. (8c) [1]. This agreement validates our PT analysis below. Furthermore, the complete overlap between the PT results including and excluding the nondipole paths indicates that the angular-integrated photoelectron yields (to the first order in $1/c$) are solely due to the interference between the absorption and emission dipole paths $P^{(\pm)}_{DD}$. This conclusion obeys the physical intuition: because the dipole (nondipole) paths have azimuthal-isotropic (azimuthal-anisotropic) continuum partial waves εs_0 and εd_0 ($\varepsilon p_{\pm 1}$ and $\varepsilon f_{\pm 1}$) according to selection rules (Fig. 1), the interference signal (to the first order in $1/c$) of the dipole paths with the nondipole paths totally cancels out in integrating along the azimuthal direction.

According to Eq. (14), the $2\omega\tau$ oscillations of the angular-integrated SB 2q signals are expressed to the first order in $1/c$ as

$$\bar{\mathcal{I}}^{2\omega}(E_{2q},\tau) \propto |\mathcal{M}^{(+)}_{DD,s}(E_{2q})||\mathcal{M}^{(-)}_{DD,s}(E_{2q})| \cos[2\omega\tau + (\phi^{(+)}_{DD,s}(E_{2q}) - \phi^{(-)}_{DD,s}(E_{2q}))] + |\mathcal{M}^{(+)}_{DD,d}(E_{2q})||\mathcal{M}^{(-)}_{DD,d}(E_{2q})| \cos[2\omega\tau + (\phi^{(+)}_{DD,d}(E_{2q}) - \phi^{(-)}_{DD,d}(E_{2q}))], \quad (15)$$

where the ensemble of the quantum numbers $\mathcal{N}$ is reduced to the angular momentum quantum number L of the final state, and the phases of the reduced ionization amplitudes are $\phi^{(\pm)}_{DD,s/d} = \arg(\mathcal{M}^{(\pm)}_{DD,s/d})$. Equation (15) indicates that, in the angular-integrated photoelectron spectra to the first order in $1/c$, the $2\omega\tau$ oscillations of SB signals only encode the interference between the same two partial waves separately from the absorption ($P^{(+)}_{DD}$) and emission ($P^{(-)}_{DD}$) dipole paths in Fig. 1, mathematically due to the orthogonality of spherical harmonics.

[3]In the TDSE simulations, the boundaries $R_c = 100.0$ and 200.0 a.u. have been separately used in the absorbing mask function $F(r) = 1 - 1/[1 + e^{(R_c - r)/4.0}]$. The convergence of time delays was found by using the larger boundary $R_c = 200.0$ a.u.

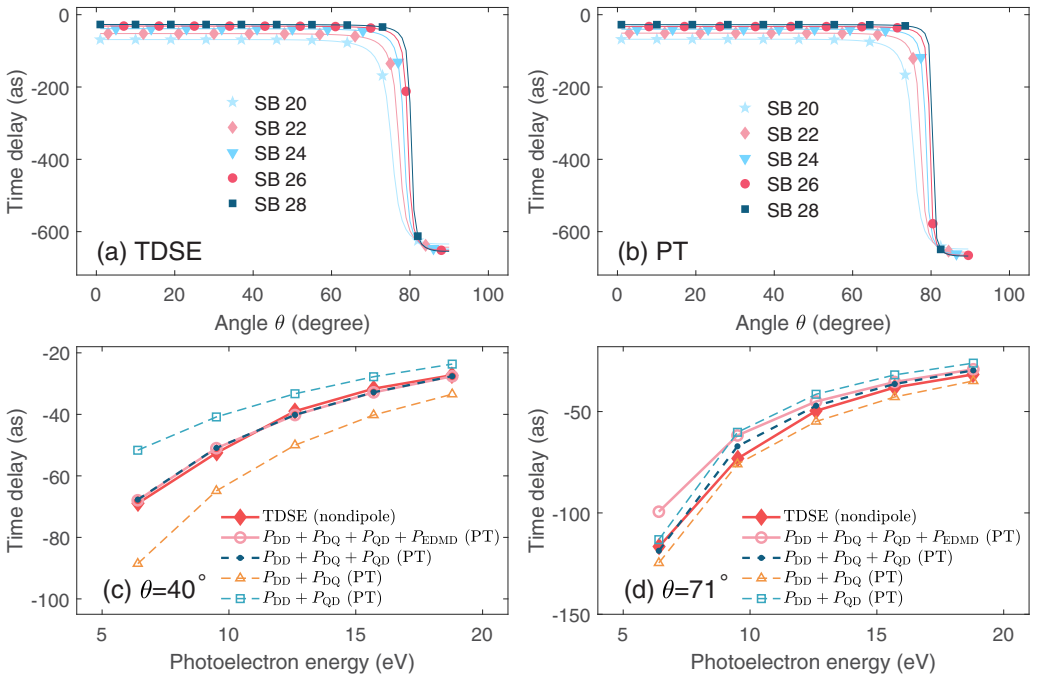

FIG. 4. (a) The photoionization time delays as a function of polar emission angle of photoelectrons for all SBs, which are extracted from the forward-backward asymmetry of the angular-resolved photoelectron spectra calculated by solving the TDSE including nondipole effects. (b) The same as (a), but calculated by PT. The stars, rhombuses, triangles, circles, and squares correspond to SBs 20, 22, 24, 26, and 28, respectively. (c) The photoionization time delay extracted from the asymmetry photoelectron spectra at polar emission angle $\theta = 40^\circ$ as a function of the photoelectron energy. (d) The same as (c), but for polar emission angle $\theta = 71^\circ$. The rhombuses correspond to the TDSE results. The circles (dots) refer to the PT results including all the paths P_{DD}, P_{DQ}, P_{QD}, and P_{EDMD} (only the paths P_{DD}, P_{DQ}, and P_{QD}). The triangles and squares refer to the PT results only including the paths P_{DD} and P_{DQ}, and only including the paths P_{DD} and P_{QD}, respectively.

Figure 4(a) shows TDSE results of the time delays extracted from the $2\omega\tau$ oscillations in the forward-backward asymmetry at different polar emission angles. The time delays are negative for all polar emission angles and for all SBs. In addition, the time delays vary gently for all polar angles except for an abrupt jump in the vicinity of $\theta \approx 80^\circ$. For comparison, we use PT to calculate the photoelectron yields of SBs 20 to 28 in angular-resolved photoelectron spectra as

$$\mathcal{I}(E_{2q},\theta,\varphi,\tau) = \left|\sum_{\mathcal{P}'} \mathcal{A}^{(+)}_{\mathcal{P}'}(E_{2q},\theta,\varphi,\tau) + \mathcal{A}^{(-)}_{\mathcal{P}'}(E_{2q},\theta,\varphi,\tau)\right|^2$$
$$= \frac{1}{p}\left|\sum_{\mathcal{P}',\mathcal{N}} e^{+i\omega\tau}\mathcal{M}^{(+)}_{\mathcal{P}',\mathcal{N}}(E_{2q})Y_{L,M}(\hat{p}) + e^{-i\omega\tau}\mathcal{M}^{(-)}_{\mathcal{P}',\mathcal{N}}(E_{2q})Y_{L,M}(\hat{p})\right|^2. \quad (16)$$

Then the forward-backward asymmetry of the photoelectron yields along the light-propagation direction $\varphi_0 = \pi/2$ is calculated as

$$\mathcal{I}_{asy}(E_{2q},\theta,\tau;\varphi_0=\pi/2) = \mathcal{I}(E_{2q},\theta,\varphi_0,\tau) - \mathcal{I}(E_{2q},\theta,\varphi_0+\pi,\tau). \quad (17)$$

Figure 4(b) shows the time delays as a function of polar emission angle of photoelectrons for SBs 20 to 28, which are extracted from the forward-backward asymmetry calculated by Eq. (17). Here the laser parameters are the same as the TDSE calculations. The PT results agree quantitatively with the TDSE results in Fig. 4(a), validating our following PT analysis of the angular-resolved time delays.

Figures 4(c) and 4(d), respectively, compare the TDSE and PT results of the time delay extracted from the $2\omega\tau$ oscillations of the forward-backward asymmetry at polar emission angles $\theta = 40^\circ$ and 71°, as a function of the photoelectron energy. In both Figs. 4(c) and 4(d), the time delays are negative and increase with the photoelectron energy. The increase of the time delays with the photoelectron energy is sharper at $\theta = 71^\circ$ than that at $\theta = 40^\circ$. For $\theta = 40^\circ$, the TDSE results agree well with the PT results including all the paths P_{DD}, P_{DQ}, P_{QD}, and P_{EDMD}. In addition, the agreement between the PT results including and excluding the magnetic-dipole paths P_{EDMD} [the circles and dots in Fig. 4(c)] indicates the dominant contribution of the electric-quadrupole paths

$P_{\rm DQ}$ and $P_{\rm QD}$. For $\theta = 71^\circ$ where the photoelectron yields are low, however, the calculated asymmetry time delays are more sensitive to the methods and to the involvement of $P_{\rm EDMD}$ paths, as indicated by Fig. 4(d). For comparison, Figs. 4(c) and 4(d) also show the time delays calculated by PT including the dipole paths and either one of the electric-quadrupole paths, i.e., by separately letting $\mathcal{P}' = \{\rm DD, DQ\}$ and $\{\rm DD, QD\}$ in Eq. (16). For both $\theta = 40^\circ$ and 71°, the time delays calculated by PT only including the $P_{\rm DD}$ and $P_{\rm DQ}$ ($P_{\rm DD}$ and $P_{\rm QD}$) paths are more (less) negative than those calculated by PT including all three paths $P_{\rm DD}$, $P_{\rm DQ}$, and $P_{\rm QD}$, as well as those calculated by TDSE. These obvious discrepancies indicate that the interferences of the dipole path $P_{\rm DD}$ with *both* nondipole paths $P_{\rm DQ}$ and $P_{\rm QD}$ have crucial contributions to the $2\omega\tau$ oscillations in the forward-backward asymmetry.

C. Wigner phases and continuum-continuum phases

As discussed in Sec. III B, to the first order in $1/c$, the angular-integrated photoelectron spectra only encode the phases of the dipole paths, while the forward-backward asymmetry imprints the phase differences between the dipole and the nondipole paths. In the following, we discuss the phases of the dipole and the electric-quadrupole paths in Fig. 1 (see Appendix C for details of magnetic-dipole paths $P_{\rm EDMD}$). Within the asymptotic approximation and neglecting the L-dependence of the CC phases [2], the phases of the reduced ionization amplitudes $\mathcal{M}^{(\pm)}_{\mathcal{P},\mathcal{N}}$ are approximately partitioned as (see Appendix D for details)

$$\begin{aligned}
\phi^{(\pm)}_{\rm DD,\lambda}(E_{2q}) &\approx -(\lambda+2)\frac{\pi}{2} + \eta_\lambda(\kappa_\pm) + \phi^{\rm D}_{\rm cc}(k,\kappa_\pm),\\
\phi^{(\pm)}_{\rm DQ,\lambda}(E_{2q}) &\approx -(\lambda+1)\frac{\pi}{2} + \eta_\lambda(\kappa_\pm) + \phi^{\rm Q}_{\rm cc}(k,\kappa_\pm),\\
\phi^{(\pm)}_{\rm QD,\lambda}(E_{2q}) &\approx -\lambda\frac{\pi}{2} + \eta_\lambda(\kappa_\pm) + \phi^{\rm D}_{\rm cc}(k,\kappa_\pm),
\end{aligned} \tag{18}$$

where the ensemble of the quantum numbers $\mathcal{N}$ is reduced to the angular momentum quantum number λ of the intermediate state. The intermediate angular momentum is $\lambda = 1$ ($\lambda = 2$) for $P_{\rm DD/DQ}$ paths ($P_{\rm QD}$ path). The momentum of the final continuum state is $k = \sqrt{2E_{2q}}$ and the momentum of the intermediate continuum state is $\kappa_\pm = \sqrt{2(E_{2q} \mp \omega)}$ for absorption and emission, respectively. The Wigner phases corresponding to BC transitions are the scattering phases $\eta_\lambda(\kappa_\pm)$ of the intermediate continuum state, which contain the short-range phase shift δ_λ and the Coulombic phase σ_λ. The CC phases are $\phi^{\rm D}_{\rm cc}(k,\kappa_\pm)$ and $\phi^{\rm Q}_{\rm cc}(k,\kappa_\pm)$ for the electric-dipole and electric-quadrupole CC transitions, respectively. Note that Eqs. (18) have included the phases introduced by the coefficients in Eqs. (11) and by the angular integrals of the reduced ionization amplitudes $\mathcal{M}^{(\pm)}_{\mathcal{P},\mathcal{N}}$. Including the long-range amplitude effects [2], the analytical expressions of the CC phases are given as (see Appendix D for details)

$$\begin{aligned}
\phi^{\rm D}_{\rm cc}(k,\kappa_\pm) = \arg&\left[\frac{(2\kappa_\pm)^{iZ/\kappa_\pm}}{(2k)^{iZ/k}}\frac{\Gamma[2+iZ(1/\kappa_\pm-1/k)]}{(\kappa_\pm-k)^{iZ(1/\kappa_\pm-1/k)}}\right]\\
&+\arg\left[1+\frac{iZ}{2}\left(\frac{1}{\kappa_\pm^2}+\frac{1}{k^2}\right)\frac{\kappa_\pm-k}{1+iZ(1/\kappa_\pm-1/k)}\right],
\end{aligned}$$

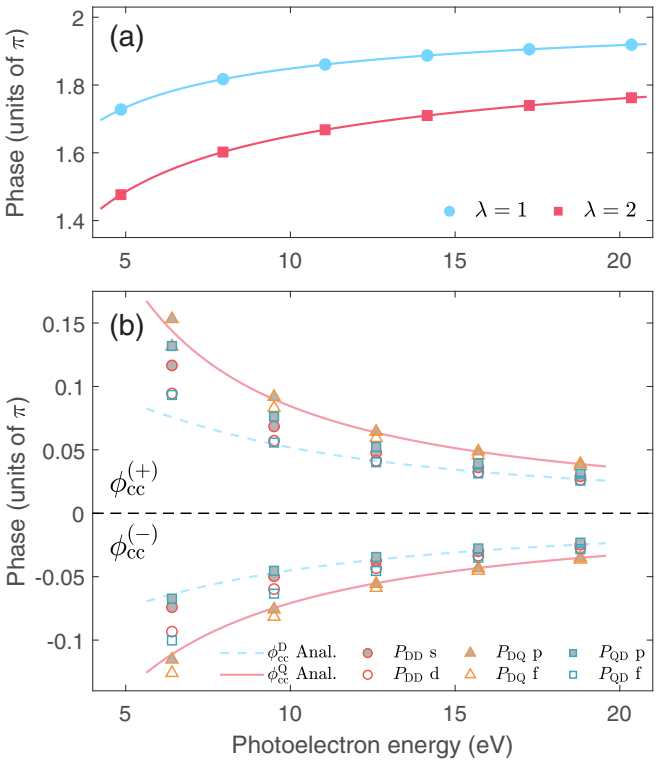

FIG. 5. (a) The Wigner phases as a function of the photoelectron energy. The circles and squares correspond to the angular momentum quantum numbers $\lambda = 1$ and 2 of the intermediate state, respectively. (b) The CC phases as a function of the photoelectron energy. The upper (lower) plane corresponds to absorption (emission) of the IR photon in the continuum. The dashed (solid) lines correspond to the analytical results for electric-dipole (electric-quadrupole) CC transitions. The circles, triangles, and squares, respectively, correspond to the paths $P_{\rm DD}$, $P_{\rm DQ}$, and $P_{\rm QD}$ in Fig. 1, with their specific partial waves indicated by the legend. The solid (hollow) symbols refer to the lower (higher) final angular momentum in each path.

$$\begin{aligned}
\phi^{\rm Q}_{\rm cc}(k,\kappa_\pm) = \arg&\left[\frac{(2\kappa_\pm)^{iZ/\kappa_\pm}}{(2k)^{iZ/k}}\frac{\Gamma[3+iZ(1/\kappa_\pm-1/k)]}{(\kappa_\pm-k)^{iZ(1/\kappa_\pm-1/k)}}\right]\\
&+\arg\left[1+\frac{iZ}{2}\left(\frac{1}{\kappa_\pm^2}+\frac{1}{k^2}\right)\frac{\kappa_\pm-k}{2+iZ(1/\kappa_\pm-1/k)}\right],
\end{aligned} \tag{19}$$

where the second terms of $\phi^{\rm D/Q}_{\rm cc}(k,\kappa_\pm)$ contain the modifications from long-range amplitude effects.

Figure 5(a) shows the Wigner phases η_λ ($\lambda = 1, 2$) as a function of the photoelectron energy for all paths in Fig. 1. The Wigner phases η_λ are positive and they increase with the photoelectron energy for all paths. The Wigner phase is larger for the $P_{\rm DD/DQ}$ ($\lambda = 1$) path with electric-dipole BC transitions at all photoelectron energies. Figure 5(b) shows the analytical CC phases calculated by Eqs. (19) as a function of the photoelectron energy. In the case of absorbing (emitting) the IR photon, the CC phases are positive (negative) and decrease (increase) with the photoelectron energy, with their values approaching zero at high photoelectron energies. In both absorption and emission cases, the

CC phases for the electric-quadrupole CC transition have a larger absolute value than those for the electric-dipole CC transition, and their difference becomes smaller with the photoelectron energy.

To examine the accuracy of the analytical expressions of the CC phases in Eqs. (19), we use PT to calculate the CC phases from the radial integral $\mathcal{R}^{(\pm)}_{\mathcal{P},\mathcal{N}}$ of the reduced transition amplitudes ($\mathcal{M}^{(\pm)}_{\mathcal{P},\mathcal{N}}$) as (see Appendix D for details)

$$\begin{aligned}\phi_{\rm cc}^{\rm DD/QD,\mathcal{N}}(k,\kappa_\pm) &= \arg(\mathcal{R}^{(\pm)}_{\rm DD/QD,\mathcal{N}}) - (L-\lambda-1)\frac{\pi}{2} - \eta_\lambda(\kappa_\pm) + \eta_L(k),\\ \phi_{\rm cc}^{\rm DQ,\mathcal{N}}(k,\kappa_\pm) &= \arg(\mathcal{R}^{(\pm)}_{\rm DQ,\mathcal{N}}) - (L-\lambda)\frac{\pi}{2} - \eta_\lambda(\kappa_\pm) + \eta_L(k) - \arg(\kappa_\pm - k),\end{aligned} \tag{20}$$

where we use $\arg(\kappa_+ - k) = 0\,[\arg(\kappa_- - k) = -\pi]$ for $\kappa_+ > k\,[\kappa_- < k]$ in the emission (absorption) case. Note that the numerical CC phases calculated by Eqs. (20) are independent of the *magnetic* quantum numbers (m_i, μ, M) of the initial, the intermediate, and the final states. Figure 5(b) shows the CC phases $\phi_{\rm cc}^{\mathcal{P},\mathcal{N}}$ calculated by Eqs. (20) as a function of the photoelectron energy. By comparing the analytical $\phi_{\rm cc}^{\rm D/Q}$ [Eqs. (19)] and the numerical $\phi_{\rm cc}^{\mathcal{P},\mathcal{N}}$ [Eqs. (20)] CC phases, we conclude that the analytical expressions of the CC phases in Eqs. (19) are more accurate for electric-quadrupole CC transitions ($P_{\rm DQ}$ paths) compared to electric-dipole CC transitions ($P_{\rm DD}$ and $P_{\rm QD}$ paths), as indicated by the smaller deviations of the numerical CC phases from the analytical ones and by the smaller L-dependencies of the numerical CC phases in Fig. 5(b). In each path, the analytical CC phases are more accurate for emission cases and at high photoelectron energies [2]. In these above cases, the asymptotic approximation works better for the perturbed wave function and the continuum wave function of the final state in the radial integrals $\mathcal{R}^{(\pm)}_{\mathcal{P},\mathcal{N}}$ [2]. Correspondingly, the approximated partition of the phases in Eqs. (18) is also more accurate.

Using the approximated phases in Eqs. (18), the $2\omega\tau$ oscillations of the SB signals in the forward-backward asymmetry are obtained as (see Appendix E for more details)

$$\begin{aligned}\mathcal{I}^{2\omega}_{\rm asy}(E_{\rm 2q},\theta,\tau;\varphi_0) \propto\ & \alpha(E_{\rm 2q},\theta;\varphi_0)\cos\left[2\omega\tau + \eta_{\lambda=1}(\kappa_+) + \phi^{\rm D}_{\rm cc}(k,\kappa_+) - \eta_{\lambda=1}(\kappa_-) - \phi^{\rm Q}_{\rm cc}(k,\kappa_-)\right]\\ &+ \beta(E_{\rm 2q},\theta;\varphi_0)\cos\left[2\omega\tau + \eta_{\lambda=1}(\kappa_+) + \phi^{\rm Q}_{\rm cc}(k,\kappa_+) - \eta_{\lambda=1}(\kappa_-) - \phi^{\rm D}_{\rm cc}(k,\kappa_-)\right]\\ &+ \gamma(E_{\rm 2q},\theta;\varphi_0)\cos\left[2\omega\tau + \eta_{\lambda=1}(\kappa_+) + \phi^{\rm D}_{\rm cc}(k,\kappa_+) - \eta_{\lambda=2}(\kappa_-) - \phi^{\rm D}_{\rm cc}(k,\kappa_-)\right]\\ &+ \zeta(E_{\rm 2q},\theta;\varphi_0)\cos\left[2\omega\tau + \eta_{\lambda=2}(\kappa_+) + \phi^{\rm D}_{\rm cc}(k,\kappa_+) - \eta_{\lambda=1}(\kappa_-) - \phi^{\rm D}_{\rm cc}(k,\kappa_-)\right],\end{aligned} \tag{21}$$

where the coefficients have the forms

$$\begin{aligned}\alpha(E_{\rm 2q},\theta;\varphi_0) &= -8\sin\varphi_0\left[\sum_{L=0,2}\left|\mathcal{M}^{(+)}_{\rm DD,L}(E_{\rm 2q})\right|\bar{Y}_{L,0}(\theta)\right]\times\left[\sum_{L=1,3}\left|\mathcal{M}^{(-)}_{\rm DQ,L}(E_{\rm 2q})\right|\bar{Y}_{L,1}(\theta)\right],\\ \beta(E_{\rm 2q},\theta;\varphi_0) &= -8\sin\varphi_0\left[\sum_{L=1,3}\left|\mathcal{M}^{(+)}_{\rm DQ,L}(E_{\rm 2q})\right|\bar{Y}_{L,1}(\theta)\right]\times\left[\sum_{L=0,2}\left|\mathcal{M}^{(-)}_{\rm DD,L}(E_{\rm 2q})\right|\bar{Y}_{L,0}(\theta)\right],\\ \gamma(E_{\rm 2q},\theta;\varphi_0) &= -8\sin\varphi_0\left[\sum_{L=0,2}\left|\mathcal{M}^{(+)}_{\rm DD,L}(E_{\rm 2q})\right|\bar{Y}_{L,0}(\theta)\right]\times\left[\sum_{L=1,3}\left|\mathcal{M}^{(-)}_{\rm QD,L}(E_{\rm 2q})\right|\bar{Y}_{L,1}(\theta)\right],\\ \zeta(E_{\rm 2q},\theta;\varphi_0) &= -8\sin\varphi_0\left[\sum_{L=1,3}\left|\mathcal{M}^{(+)}_{\rm QD,L}(E_{\rm 2q})\right|\bar{Y}_{L,1}(\theta)\right]\times\left[\sum_{L=0,2}\left|\mathcal{M}^{(-)}_{\rm DD,L}(E_{\rm 2q})\right|\bar{Y}_{L,0}(\theta)\right],\end{aligned} \tag{22}$$

with $\varphi_0 = \pi/2$ referring to the light-propagation direction, and the ensemble of the quantum numbers $\mathcal{N}$ is reduced to the angular momentum quantum number L of the final state. Here the relation $\bar{Y}_{l,-m}(\theta) = (-1)^m\bar{Y}_{l,m}(\theta)$ is used with $Y_{l,m}(\theta,\varphi) = \bar{Y}_{l,m}(\theta)e^{im\varphi}$.

In Eq. (21), the first and second (third and fourth) terms correspond to the interference of the dipole path $P_{\rm DD}$ with the nondipole path $P_{\rm DQ}$ ($P_{\rm QD}$). In addition, the nondipole paths $P_{\rm DQ}$ and $P_{\rm QD}$ carry different phases in their interference with the dipole path, because both BC [Fig. 5(a)] and CC [Fig. 5(b)] transitions have different phases between the electric-dipole and electric-quadrupole cases. Due to their compensation, the measured time delays are in between the PT results only including the dipole paths $P_{\rm DD}$ and either of the nondipole paths $P_{\rm DQ}$ or $P_{\rm QD}$, as shown in Figs. 4(c) and 4(d). These different phases explain the discrepancies among

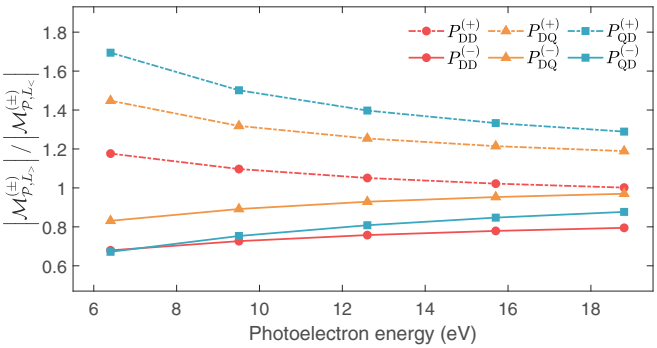

FIG. 6. The ratios of the modules of the reduced ionization amplitudes $\mathcal{M}_{\mathcal{P},\mathcal{N}}^{(\pm)}$ with a larger final angular momentum $L_>$ to those with a smaller final angular momentum $L_<$ for all paths in Fig. 1, as a function of the photoelectron energy. The dashed (solid) lines correspond to the absorption (emission) of the IR photon in the continuum. The circles, triangles, and squares refer to the paths P_{DD}, P_{DQ}, and P_{QD}, respectively.

the PT results including different sets of paths in Figs. 4(c) and 4(d). Note that the interferences of the dipole paths with the magnetic-dipole paths P_{EDMD} are omitted in Eq. (21) for their small contribution. The modification from magnetic-dipole paths P_{EDMD} is given in Appendix C.

Furthermore, the coefficients in Eq. (22) depend on polar angle, which explains the difference between the asymmetry time delays at different polar angles, as seen by comparing Figs. 4(c) and 4(d). Note that the time delays extracted from the asymmetry of the photoelectron yields are independent of the choice of the asymmetry direction $\varphi = \varphi_0$ ($\varphi_0 \neq 0, \pi$) because the coefficients in Eq. (22) are all proportional to the factor $\sin\varphi_0 \neq 0$, which is verified by our TDSE and PT calculations (not shown). Here we chose the light-propagation direction ($\varphi_0 = \pi/2$) for the maximal signal-to-noise ratio.

D. The propensity rule in laser-assisted photoionization

Figure 6 shows the ratios of the modules of the reduced ionization amplitudes $\mathcal{M}_{\mathcal{P},\mathcal{N}}^{(\pm)}$ with larger ($L_>$) and smaller ($L_<$) angular quantum numbers of the final states for all paths in Fig. 1 as a function of the photoelectron energy. For all dipole and nondipole paths, the electrons are prone to increase (decrease) its angular momentum in absorbing (emitting) an IR photon in the continuum [80,81], as indicated by $|\mathcal{M}_{\mathcal{P},L_>}^{(+)}|/|\mathcal{M}_{\mathcal{P},L_<}^{(+)}| > 1$ ($|\mathcal{M}_{\mathcal{P},L_>}^{(-)}|/|\mathcal{M}_{\mathcal{P},L_<}^{(-)}| < 1$) at all photoelectron energies in Fig. 6. Moreover, this propensity for increasing or decreasing the angular momentum becomes less with the photoelectron energy for all paths, with the ratio $|\mathcal{M}_{\mathcal{P},L_>}^{(\pm)}|/|\mathcal{M}_{\mathcal{P},L_<}^{(\pm)}|$ approaching the ratio of their angular integrals [81]. In addition, Fig. 6 indicates that different paths have different degrees of propensity towards increasing or decreasing the angular momentum: $P_{QD} > P_{DQ} > P_{DD}$ for absorption (the ratios $|\mathcal{M}_{\mathcal{P},L_>}^{(+)}|/|\mathcal{M}_{\mathcal{P},L_<}^{(+)}|$ from the biggest to the smallest) while $P_{DD} > P_{QD} > P_{DQ}$ (the ratios $|\mathcal{M}_{\mathcal{P},L_>}^{(-)}|/|\mathcal{M}_{\mathcal{P},L_<}^{(-)}|$ from the smallest to the biggest) for emission.

In the following, we use the propensity rule in Fig. 6 to interpret the abrupt jump of the angular-resolved asymmetry time delays in Figs. 4(a) and 4(b). In P_{DQ} and P_{QD} cases (P_{DD} case), $\varepsilon f_{\pm 1}$ waves (εd_0 wave) change(s) into negative signs crossing their (its) node at polar angle $\theta \approx 63.4^\circ$ ($\theta \approx 54.5^\circ$), and thus destructively interfere(s) with the positive $\varepsilon p_{\pm 1}$ waves (εs_0 wave), as shown in Fig. 1. Furthermore, in the absorption case for all paths, the negative partial waves $\varepsilon f_{\pm 1}$ and εd_0 have a bigger amplitude, with their higher angular momenta, and thus they completely cancel the positive partial waves $\varepsilon p_{\pm 1}$ and εs_0 when interfering. Therefore, the coefficients α, β, γ, and ζ in Eqs. (22) exhibit values of zero near polar angle $\theta \approx 80^\circ$ due to the competition of the partial waves in paths $P_{DD}^{(+)}$, $P_{DQ}^{(+)}$, $P_{DD}^{(+)}$, and $P_{QD}^{(+)}$, respectively. Correspondingly, sudden jumps occur in the time delays near the zeros of the coefficients in Figs. 4(a) and 4(b).

IV. CONCLUSION

We have systematically investigated the nondipole RABBIT measurement on an atom using linearly polarized XUV and IR fields. By scanning the time delay τ between the XUV and IR fields, we calculated the three-dimensional photoelectron spectra to the first order in $1/c$ by solving the TDSE and by PT within the single-active-electron approximation. In the RABBIT scheme beyond the DA, either of the BC and CC transitions can be electric-dipole or electric-quadrupole in two-photon transitions, resulting in isotropic (anisotropic) continuum partial waves along the azimuthal direction for dipole-dipole (dipole-quadrupole and quadrupole-dipole) paths.

In the photoelectron spectra integrated over both polar and azimuthal emission angles of photoelectrons (to the first order in $1/c$), the $2\omega\tau$ oscillations of the SB signals originate purely from the interference among the absorption and emission dipole-dipole paths, due to the cancellation of the azimuthal-*anisotropic* continuum partial waves of dipole-quadrupole and quadrupole-dipole paths in their interference with the azimuthal-*isotropic* continuum partial waves of dipole-dipole paths. In the asymmetry of the photoelectron spectra along the light-propagation direction (to the first order in $1/c$), the $2\omega\tau$ oscillations of the SB signals mainly result from the interference of dipole-dipole paths with dipole-quadrupole and quadrupole-dipole paths. Hence, the time delays retrieved from the modulating forward-backward asymmetry reveal nondipole effects on the electronic dynamics in photoionization. Furthermore, the extracted time delays exhibit an abrupt jump in the vicinity of polar angle $\theta \approx 80^\circ$ due to the competition among the partial waves in the absorption paths for both dipole and nondipole cases.

Similar to conventional RABBIT within the DA, the retrieved RABBIT phases can be approximately separated into Wigner and CC phases, respectively, corresponding to the BC and CC transitions in two-photon above-threshold ionization including nondipole effects (assuming zero phases of XUV harmonics and in the absence of resonances). Our PT calculations revealed that dipole-quadrupole and quadrupole-dipole paths had different photoionization time delays due to their different Wigner and CC phases. Moreover, electrons prefer to increase (decrease) the angular momentum in absorbing (emitting) an IR photon in the continuum in the case of nondipole two-photon above-threshold ionization, in

accordance with the propensity rule in laser-assisted photoionization within the DA.

We discussed nondipole effects in the RABBIT measurement on an atom using linearly polarized laser fields. We believe that underlying physics can be generalized to the nondipole RABBIT using circularly polarized fields and to more complex molecular [87] systems.

ACKNOWLEDGMENTS

This work was supported by the National Key Research and Development Program of China (Grant No. 2019YFA0308300), National Natural Science Foundation of China (Grants No. 12374264, No. 12021004, and No. 92250303), and Shaanxi Science Foundation (Grant No. 2022JC-DW-05). J.M.D. acknowledges support from the Knut and Alice Wallenberg Foundation (Grant No. 2019.0154) and the Olle Engkvist's Foundation (Grant No. 194-0734). The computing work in this paper is supported by the Public Service Platform of High Performance Computing provided by Network and Computing Center of HUST.

Y.L. and Y.C. contributed equally to this work.

APPENDIX A: THE HAMILTONIAN IN THE NONDIPOLE TDSE

Using $\mathbf{A}(\mathbf{r},t)=\mathbf{A}(\xi=t-\hat{k}\cdot\mathbf{r}/c)\approx\mathbf{A}(t)-(\hat{k}\cdot\mathbf{r}/c)d\mathbf{A}(t)/dt$ and $\mathbf{E}(t)=-d\mathbf{A}(t)/dt$ for the electric field, the Hamiltonian in Eq. (2) is expanded to the first order in $1/c$ as [55,66]

$$H=\frac{1}{2}[\mathbf{p}+\mathbf{A}(t)]^2+\frac{1}{c}(\hat{k}\cdot\mathbf{r})[\mathbf{p}+\mathbf{A}(t)]\cdot\mathbf{E}(t)+V(\mathbf{r}). \tag{A1}$$

To dismiss the direct coupling between the position operator $\mathbf{r}$ and the momentum operator $\mathbf{p}$, we apply a unitary transformation $U=\exp(-i\chi)$ with a Hermitian operator $\chi=(\hat{k}\cdot\mathbf{r})(\mathbf{p}\cdot\mathbf{A}(t)+\frac{1}{2}\mathbf{A}^2(t))/c$ [55], which leads to a transformed wave function $\widetilde{\Psi}=U\Psi$ and the transformed Hamiltonian to the first order in $1/c$ (using the Baker-Campbell-Hausdorff formula $e^XYe^{-X}=Y+[X,Y]+[X,[X,Y]]/2!+[X,[X,[X,Y]]]/3!+\cdots$) [55]

$$\begin{aligned}\widetilde{H}&=UHU^\dagger+i\frac{\partial U}{\partial t}U^\dagger=UHU^\dagger+\frac{\partial}{\partial t}\chi\approx\frac{1}{2}\left[\mathbf{p}+\frac{\hat{k}}{c}\left(\mathbf{p}\cdot\mathbf{A}(t)+\frac{1}{2}\mathbf{A}^2(t)\right)+\mathbf{A}(t)\right]^2+V\left(\mathbf{r}-\frac{1}{c}(\hat{k}\cdot\mathbf{r})\mathbf{A}(t)\right)\\&\approx\frac{1}{2}\left[\mathbf{p}^2+\mathbf{p}\cdot\mathbf{A}(t)+\mathbf{A}(t)\cdot\mathbf{p}+\frac{1}{c}(\hat{k}\cdot\mathbf{p})\left(\mathbf{p}\cdot\mathbf{A}(t)+\frac{1}{2}\mathbf{A}^2(t)\right)+\frac{1}{c}\left(\mathbf{p}\cdot\mathbf{A}(t)+\frac{1}{2}\mathbf{A}^2(t)\right)(\hat{k}\cdot\mathbf{p})+\mathbf{A}^2(t)\right]\\&\quad+V\left(\mathbf{r}-\frac{1}{c}(\hat{k}\cdot\mathbf{r})\mathbf{A}(t)\right).\end{aligned} \tag{A2}$$

Here we used the relation $\hat{\epsilon}\cdot\hat{k}=0$. This unitary transformation can be interpreted as the shifts of position and momentum operators,

$$\mathbf{r}\to\widetilde{\mathbf{r}}=\mathbf{r}-\frac{1}{c}(\hat{k}\cdot\mathbf{r})\mathbf{A}(t),\ \ \mathbf{p}\to\widetilde{\mathbf{p}}=\mathbf{p}+\frac{\hat{k}}{c}\left(\mathbf{p}\cdot\mathbf{A}(t)+\frac{1}{2}\mathbf{A}^2(t)\right). \tag{A3}$$

Then the Hamiltonian in Eq. (A2) is further transformed into "velocity gauge" by [52]

$$\mathbf{A}\to\mathbf{A}'=\mathbf{A}+\nabla f,\ \ \phi\to\phi'=\phi-\partial f/\partial t,\ \ \Psi\to\Psi'=\exp(-if)\Psi, \tag{A4a}$$

$$f=\int_{-\infty}^{t}\frac{1}{2}\mathbf{A}^2(t')dt', \tag{A4b}$$

where $\mathbf{A}$, ϕ, and Ψ are the vector potential, the scalar potential, and the wave function, respectively. In Coulomb gauge ($\nabla\cdot\mathbf{A}=\mathbf{0}$ or $[\mathbf{p},\mathbf{A}]=\mathbf{0}$), the Hamiltonian is obtained as

$$H=\frac{1}{2}\mathbf{p}^2+\mathbf{p}\cdot\mathbf{A}(t)+\frac{1}{c}(\hat{k}\cdot\mathbf{p})\left(\mathbf{p}\cdot\mathbf{A}(t)+\frac{1}{2}\mathbf{A}^2(t)\right)+V\left(\mathbf{r}-\frac{1}{c}(\hat{k}\cdot\mathbf{r})\mathbf{A}(t)\right). \tag{A5}$$

To speed up the time propagation, the shifted potential is expanded to the first order in $1/c$ as $V(\mathbf{r}-(\hat{k}\cdot\mathbf{r}/c)\mathbf{A}(t))\approx V(\mathbf{r})-(\hat{k}\cdot\mathbf{r})\mathbf{A}(t)\cdot\nabla V(\mathbf{r})/c$ [55], which gives the Hamiltonian in Eq. (3).

APPENDIX B: THE DERIVATIONS FOR SINGLE- AND TWO-PHOTON TRANSITION MOMENTS INCLUDING NONDIPOLE EFFECTS

Applying the gauge transformation to the Hamiltonian in Eq. (A1) with the function $f=-\mathbf{A}(t)\cdot\mathbf{r}$ in Eq. (A4a), we obtain the Hamiltonian in "length gauge" as [66,75] $H=H_0+H_{\rm int}^{\rm L}$, with the atomic Hamiltonian $H_0=\mathbf{p}^2/2+V(\mathbf{r})$. The laser-atom interaction term is

$$H_{\rm int}^{\rm L}=\left[\mathbf{r}+\frac{1}{c}(\hat{k}\cdot\mathbf{r})\mathbf{p}\right]\cdot\mathbf{E}(t)=H_{\rm int}^{\rm D}+H_{\rm int}^{\rm ND}, \tag{B1}$$

where the electric-dipole contribution is $H_{\rm int}^{\rm D} = \mathbf{E}(t)\cdot\mathbf{r} = E(t)\hat{O}_{\rm ED}$ and the nondipole contribution is $H_{\rm int}^{\rm ND} = (\hat{k}\cdot\mathbf{r})\mathbf{E}(t)\cdot\mathbf{p}/c = E(t)\hat{O}_{\rm ND}/c$. The transition operator is $\hat{O} = \hat{O}_{\rm ED} + \hat{O}_{\rm ND}/c$, which contains the electric-dipole $\hat{O}_{\rm ED} = \hat{\epsilon}\cdot\mathbf{r}$ and the nondipole $\hat{O}_{\rm ND} = (\hat{k}\cdot\mathbf{r})(\hat{\epsilon}\cdot\mathbf{p})$ contributions.

In partitioning electric-quadrupole and magnetic-dipole contributions, we use the commutator $\mathbf{p} = i[H_0, \mathbf{r}]$ and the relation $(\hat{k}\cdot\mathbf{p})(\hat{\epsilon}\cdot\mathbf{r}) = (\hat{\epsilon}\cdot\mathbf{p})(\hat{k}\cdot\mathbf{r}) + (\hat{\epsilon}\times\hat{k})\cdot(\mathbf{r}\times\mathbf{p})$ to transform the nondipole *one-photon* transition moment $\langle\psi_n|\hat{O}_{\rm ND}|\psi_m\rangle$ between two atomic states into pure position representation:

$$\begin{aligned}
\langle\psi_n|\hat{O}_{\rm ND}|\psi_m\rangle &= \langle\psi_n|(\hat{k}\cdot\mathbf{r})(\hat{\epsilon}\cdot\mathbf{p})|\psi_m\rangle = i\langle\psi_n|(\hat{k}\cdot\mathbf{r})H_0(\hat{\epsilon}\cdot\mathbf{r})|\psi_m\rangle - i\langle\psi_n|(\hat{k}\cdot\mathbf{r})(\hat{\epsilon}\cdot\mathbf{r})H_0|\psi_m\rangle \\
&= -\langle\psi_n|(\hat{k}\cdot\mathbf{p})(\hat{\epsilon}\cdot\mathbf{r})|\psi_m\rangle + i\langle\psi_n|H_0(\hat{k}\cdot\mathbf{r})(\hat{\epsilon}\cdot\mathbf{r})|\psi_m\rangle - i\omega_m\langle\psi_n|(\hat{k}\cdot\mathbf{r})(\hat{\epsilon}\cdot\mathbf{r})|\psi_m\rangle \\
&= -\langle\psi_n|(\hat{k}\cdot\mathbf{r})(\hat{\epsilon}\cdot\mathbf{p})|\psi_m\rangle - \langle\psi_n|(\hat{\epsilon}\times\hat{k})\cdot(\mathbf{r}\times\mathbf{p})|\psi_m\rangle + i(\omega_n-\omega_m)\langle\psi_n|(\hat{k}\cdot\mathbf{r})(\hat{\epsilon}\cdot\mathbf{r})|\psi_m\rangle \\
&= \frac{i}{2}(\omega_n-\omega_m)\langle\psi_n|(\hat{k}\cdot\mathbf{r})(\hat{\epsilon}\cdot\mathbf{r})|\psi_m\rangle + \frac{1}{2}\langle\psi_n|(\hat{k}\times\hat{\epsilon})\cdot(\mathbf{r}\times\mathbf{p})|\psi_m\rangle \\
&= \frac{i}{2}(\omega_n-\omega_m)\langle\psi_n|\hat{O}_{\rm EQ}|\psi_m\rangle + \frac{1}{2}\langle\psi_n|\hat{O}_{\rm MD}|\psi_m\rangle,
\end{aligned}$$

where the denotations are given in Sec. II B. Note that the energy difference is $\omega_n - \omega_m > 0$ ($\omega_n - \omega_m < 0$) for absorption (emission). Our results are consistent with changing the interaction term within the DA, $\mathbf{p}\cdot\mathbf{A}(t)$ into that beyond the DA, $\mathbf{p}\cdot\mathbf{A}(t)e^{\pm i\mathbf{k}\cdot\mathbf{r}}$, in velocity gauge (+ for absorption and − for emission), as done in Refs. [47,88,89].

According to Eq. (B1), the *two-photon* transition moments from the initial state $|\psi_i\rangle$ to the final state $|\psi_f\rangle$ can include one step of a nondipole transition either after a dipole transition [17]

$$\mathcal{M}^{(2)}_{\rm D+ND} = \langle\psi_f|\hat{O}_{\rm ND}G^+(\omega')\hat{O}_{\rm ED}|\psi_i\rangle, \tag{B2}$$

or before a dipole transition

$$\mathcal{M}^{(2)}_{\rm ND+D} = \langle\psi_f|\hat{O}_{\rm ED}G^+(\omega')\hat{O}_{\rm ND}|\psi_i\rangle, \tag{B3}$$

with $\omega' = \omega_i + \Omega$ and $\mathcal{M}^{(2)}_{\rm D+ND/ND+D}$ the reduced transition amplitudes. The retarded (G^+) and advanced (G^-) resolvents for the field-free system H_0 are expanded on the atomic states as [90]

$$G^\pm(\omega') = (\omega' - H_0 \pm i0^+)^{-1} = \sum\!\!\!\!\!\!\int_v \frac{|\psi_v\rangle\langle\psi_v|}{\omega'-\omega_v\pm i0^+}, \tag{B4}$$

with $H_0|\psi_v\rangle = \omega_v|\psi_v\rangle$. Here the resolvents satisfy the relations $(G^+)^\dagger = G^-$ and $(G^\pm)^{-1} = \omega' - H_0 \pm i0^+$. Alternatively, the reduced nondipole transition amplitudes $\mathcal{M}^{(2)}_{\rm D+ND/ND+D}$ can be expressed as [2,85]

$$\begin{aligned}
\mathcal{M}^{(2)}_{\rm D+ND} &= \frac{1}{c}\langle\rho_f^-|\hat{O}_{\rm ED}|\psi_i\rangle, \\
\mathcal{M}^{(2)}_{\rm ND+D} &= \frac{1}{c}\langle\psi_f|\hat{O}_{\rm ED}|\rho_i^+\rangle,
\end{aligned} \tag{B5}$$

where the forward- ($|\rho_\beta^+\rangle$) and backward-propagating ($\langle\rho_\beta^-|$) perturbed wave functions are defined as $|\rho_\beta^\pm\rangle = G^\pm(\omega')(\hat{k}\cdot\mathbf{r})(\hat{\epsilon}\cdot\mathbf{p})|\psi_\beta\rangle$ ($\beta = i, f$). Likewise, we can transform $|\rho_\beta^\pm\rangle$ into pure position representation:

$$\begin{aligned}
|\rho_\beta^\pm\rangle &= G^\pm(\omega')(\hat{k}\cdot\mathbf{r})(\hat{\epsilon}\cdot\mathbf{p})|\psi_\beta\rangle = -iG^\pm(\omega')(\hat{k}\cdot\mathbf{r})(\hat{\epsilon}\cdot\mathbf{r})H_0|\psi_\beta\rangle + iG^\pm(\omega')(\hat{k}\cdot\mathbf{r})H_0(\hat{\epsilon}\cdot\mathbf{r})|\psi_\beta\rangle \\
&= -i\omega_\beta G^\pm(\omega')(\hat{k}\cdot\mathbf{r})(\hat{\epsilon}\cdot\mathbf{r})|\psi_\beta\rangle - G^\pm(\omega')(\hat{k}\cdot\mathbf{p})(\hat{\epsilon}\cdot\mathbf{r})|\psi_\beta\rangle + iG^\pm(\omega')H_0(\hat{k}\cdot\mathbf{r})(\hat{\epsilon}\cdot\mathbf{r})|\psi_\beta\rangle \\
&= i(\omega'-\omega_\beta)G^\pm(\omega')(\hat{k}\cdot\mathbf{r})(\hat{\epsilon}\cdot\mathbf{r})|\psi_\beta\rangle - G^\pm(\omega')(\hat{k}\cdot\mathbf{p})(\hat{\epsilon}\cdot\mathbf{r})|\psi_\beta\rangle - iG^\pm(\omega')(\omega' - H_0 \pm i0^+)(\hat{k}\cdot\mathbf{r})(\hat{\epsilon}\cdot\mathbf{r})|\psi_\beta\rangle \\
&= i(\omega'-\omega_\beta)G^\pm(\omega')(\hat{k}\cdot\mathbf{r})(\hat{\epsilon}\cdot\mathbf{r})|\psi_\beta\rangle - G^\pm(\omega')(\hat{k}\cdot\mathbf{r})(\hat{\epsilon}\cdot\mathbf{p})|\psi_\beta\rangle - G^\pm(\omega')(\hat{\epsilon}\times\hat{k})\cdot(\mathbf{r}\times\mathbf{p})|\psi_\beta\rangle - i(\hat{k}\cdot\mathbf{r})(\hat{\epsilon}\cdot\mathbf{r})|\psi_\beta\rangle \\
&= \frac{i}{2}(\omega'-\omega_\beta)G^\pm(\omega')\hat{O}_{\rm EQ}|\psi_\beta\rangle + \frac{1}{2}G^\pm(\omega')\hat{O}_{\rm MD}|\psi_\beta\rangle - \frac{i}{2}(\hat{k}\cdot\mathbf{r})(\hat{\epsilon}\cdot\mathbf{r})|\psi_\beta\rangle \\
&\approx \frac{i}{2}(\omega'-\omega_\beta)G^\pm(\omega')\hat{O}_{\rm EQ}|\psi_\beta\rangle + \frac{1}{2}G^\pm(\omega')\hat{O}_{\rm MD}|\psi_\beta\rangle,
\end{aligned}$$

with $\omega' - \omega_\beta = i\Omega$ ($\omega' - \omega_\beta = \mp i\omega$) for $\beta = i$ ($\beta = f$). In the last step, the term "$(\hat{k}\cdot\mathbf{r})(\hat{\epsilon}\cdot\mathbf{r})|\psi_\beta\rangle$" is safely neglected because it physically means the simultaneous exchange of one electric-dipole photon plus one electric-quadrupole photon, with much lower possibilities than the two-photon transitions via virtual states (three orders lower in our calculations). Note that our results are consistent with the interaction term in Eq. (9) as a correspondence of the Hamiltonian under Power-Zienau-Woolley transform in the quantum electrodynamics framework [74,77].

APPENDIX C: THE ELECTRIC-DIPOLE–MAGNETIC-DIPOLE PATHS IN TWO-PHOTON ABOVE-THRESHOLD IONIZATION

With the monochromatic approximation, the two-photon ionization amplitudes, corresponding to the electric-dipole BC and the magnetic-dipole CC transitions, are given as

$$\begin{aligned}\mathcal{A}^{(\pm)}_{\mathrm{EDMD}}(E_{2\mathrm{q}},\theta,\varphi,\tau) &= -\frac{i}{8c}E_\omega E_\Omega e^{\pm i\omega\tau+i\phi_\Omega}\sum\!\!\!\!\!\!\int_\nu \frac{\langle\psi_f|\hat{O}_{\mathrm{MD}}|\psi_\nu\rangle\langle\psi_\nu|\hat{O}_{\mathrm{ED}}|\psi_i\rangle}{\omega_i+\Omega-\omega_\nu+i0^+}\\ &= \frac{1}{p^{1/2}}\sum_{\mathcal{N}} e^{\pm i\omega\tau+i\phi_\Omega}\mathcal{M}^{(\pm)}_{\mathrm{EDMD},\mathcal{N}}(E_{2\mathrm{q}})Y_{L,M}(\hat{p}),\end{aligned} \tag{C1}$$

where the denotations are given in Sec. II B. The magnetic-dipole transition operator is $\hat{O}_{\mathrm{MD}} = L_x = (L_+ + L_-)/2$ in our calculations, with $L_\pm$ the ladder operators $L_\pm Y_{l,m} = \sqrt{l(l+1)-m(m\pm1)}Y_{l,m\pm1}$. According to the selection rules, the electric-dipole–magnetic-dipole (ED-MD) paths have the ionization channels $s_0 \to p_0 \to \varepsilon p_{\pm1}$ in both absorption and emission cases. The reduced ionization amplitudes for the ED-MD paths are obtained as

$$\begin{aligned}\mathcal{M}^{(\pm)}_{\mathrm{EDMD},\mathcal{N}} &= -\frac{i^{-(L-1)}e^{i\eta_L}}{16c}E_\omega E_\Omega \sum\!\!\!\!\!\!\int_\nu \frac{\langle R_{E,L}|R_{\nu,\lambda}\rangle\langle R_{\nu,\lambda}|r|R_{n_i,l_i}\rangle}{\omega_i+\Omega-\omega_\nu+i0^+}\times\langle Y_{L,M}|L_{+/-}|Y_{\lambda,\mu}\rangle\langle Y_{\lambda,\mu}|Y_{1,0}|Y_{l_i,m_i}\rangle\\ &= \pm\frac{i^{-(L-1)}e^{i\eta_L}}{8\sqrt{2}c\omega}E_\omega E_\Omega\langle R_{E,L}|r|R_{n_i,l_i}\rangle\times\langle Y_{L,M}|Y_{\lambda,\mu+1/\mu-1}\rangle\langle Y_{\lambda,\mu}|Y_{1,0}|Y_{l_i,m_i}\rangle,\end{aligned} \tag{C2}$$

where the ensemble of the quantum numbers $\mathcal{N}$ is reduced to the angular momentum quantum number $L=1$ of the final state for both emission and absorption cases because the amplitudes $\mathcal{M}^{(\pm)}_{\mathrm{EDMD},\mathcal{N}}$ are the same for the magnetic quantum number $M=\pm1$ of the final state.

Like the electric-quadrupole paths $P_{\mathrm{DQ/QD}}$, the interference of the ED-MD paths P_{EDMD} with the dipole paths P_{DD} leads to the $2\omega\tau$ oscillations of the SB 2q signal to the first order in $1/c$:

$$\begin{aligned}\mathcal{I}^{\mathrm{M},2\omega}(E_{2\mathrm{q}},\theta,\varphi,\tau) \propto 2\sum_{L=0,2}\sum_{M'=\pm1}&\bar{Y}_{L,M=0}(\theta)\bar{Y}_{L'=1,M'}(\theta)\\ &\{-|\mathcal{M}^{(+)}_{\mathrm{DD,L}}(E_{2\mathrm{q}})||\mathcal{Q}^{(-)}_{\mathrm{DD,L'=1}}(E_{2\mathrm{q}})|\cos[2\omega\tau+\phi^{(+)}_{\mathrm{DD,L}}(E_{2\mathrm{q}})-\eta_{L'=1}(E_{2\mathrm{q}})-M'\varphi]\\ &+|\mathcal{M}^{(-)}_{\mathrm{DD,L}}(E_{2\mathrm{q}})||\mathcal{Q}^{(+)}_{\mathrm{DD,L'=1}}(E_{2\mathrm{q}})|\cos[2\omega\tau+\eta_{L'=1}(E_{2\mathrm{q}})-\phi^{(-)}_{\mathrm{DD,L}}(E_{2\mathrm{q}})+M'\varphi]\},\end{aligned} \tag{C3}$$

where the denotations are given in Sec. III B. In the corresponding forward-backward asymmetry of the photoelectron yields along the direction $\varphi=\varphi_0$, the $2\omega\tau$ oscillations of the SB 2q signal are obtained as (following similar derivations in Appendix E)

$$\begin{aligned}\mathcal{I}^{\mathrm{M},2\omega}_{\mathrm{asy}}(E_{2\mathrm{q}},\theta,\tau;\varphi_0) &= \mathcal{I}^{\mathrm{M},2\omega}(E_{2\mathrm{q}},\theta,\varphi_0,\tau)-\mathcal{I}^{\mathrm{M},2\omega}(E_{2\mathrm{q}},\theta,\varphi_0+\pi,\tau)\\ &\propto 4\sum_{L=0,2}\sum_{M'=\pm1}\bar{Y}_{L,0}(\theta)\bar{Y}_{1,M'}(\theta)\{-|\mathcal{M}^{(+)}_{\mathrm{DD,L}}(E_{2\mathrm{q}})||\mathcal{Q}^{(-)}_{\mathrm{DD,L'=1}}(E_{2\mathrm{q}})|\cos[2\omega\tau+\phi^{(+)}_{\mathrm{DD,L}}(E_{2\mathrm{q}})-\eta_{L'=1}(E_{2\mathrm{q}})-M'\varphi_0]\\ &\quad+|\mathcal{M}^{(-)}_{\mathrm{DD,L}}(E_{2\mathrm{q}})||\mathcal{Q}^{(+)}_{\mathrm{DD,L'=1}}(E_{2\mathrm{q}})|\cos[2\omega\tau+\eta_{L'=1}(E_{2\mathrm{q}})-\phi^{(-)}_{\mathrm{DD,L}}(E_{2\mathrm{q}})+M'\varphi_0]\}\\ &= -8\sin\varphi_0\bar{Y}_{1,1}(\theta)\sum_{L=0,2}\bar{Y}_{L,0}(\theta)\{|\mathcal{M}^{(+)}_{\mathrm{DD,L}}(E_{2\mathrm{q}})||\mathcal{Q}^{(-)}_{\mathrm{DD,L'=1}}(E_{2\mathrm{q}})|\sin[2\omega\tau+\phi^{(+)}_{\mathrm{DD,L}}(E_{2\mathrm{q}})-\eta_{\mathrm{p}}(E_{2\mathrm{q}})]\\ &\quad+|\mathcal{M}^{(-)}_{\mathrm{DD,L}}(E_{2\mathrm{q}})||\mathcal{Q}^{(+)}_{\mathrm{DD,L'=1}}(E_{2\mathrm{q}})|\sin[2\omega\tau+\eta_{L'=1}(E_{2\mathrm{q}})-\phi^{(-)}_{\mathrm{DD,L}}(E_{2\mathrm{q}})]\}.\end{aligned} \tag{C4}$$

APPENDIX D: THE DERIVATIONS FOR THE PHASES OF THE TWO-PHOTON TRANSITIONS INCLUDING NONDIPOLE EFFECTS

In this Appendix, we will derive the phases of P_{DQ} and P_{QD} paths following Ref. [2]. The radial integrals, $\mathcal{R}^{(\pm)}_{\mathrm{DQ/QD},\mathcal{N}}$, of the reduced transition amplitudes ($\mathcal{M}^{(\pm)}_{\mathrm{DQ/QD},\mathcal{N}}$) are

$$\begin{aligned}\mathcal{R}^{(\pm)}_{\mathrm{DQ},\mathcal{N}} &= \sum\!\!\!\!\!\!\int_\nu \frac{\langle R_{k,L}|r^2|R_{\nu,\lambda}\rangle\langle R_{\nu,\lambda}|r\big|R_{n_i,l_i}\rangle}{\omega_i+\Omega-\omega_\nu+i0^+},\\ \mathcal{R}^{(\pm)}_{\mathrm{QD},\mathcal{N}} &= \sum\!\!\!\!\!\!\int_\nu \frac{\langle R_{k,L}|r|R_{\nu,\lambda}\rangle\langle R_{\nu,\lambda}|r^2\big|R_{n_i,l_i}\rangle}{\omega_i+\Omega-\omega_\nu+i0^+},\end{aligned} \tag{D1}$$

where R_{n_i,l_i}, $R_{\nu,\lambda}$, and $R_{k,L}$ are the radial wave functions of the initial, the intermediate, and the final states, respectively. The final scattering wave $R_{k,L}$ has the asymptotic behavior at infinite r as $R_{k,L}(r) \to \frac{N_k}{r}\sin[\Phi_{k,L}(r)]$, with the amplitude

$N_k \approx \sqrt{2/(\pi k)}[1 - Z/(2rk^2)]$ within the Wentzel-Kramers-Brillouin (WKB) approximation and the phase $\Phi_{k,L}(r) = kr + Z\ln(2kr)/k + \eta_L(k) - \pi L/2$. Following Refs. [2,85], the corresponding perturbed wave functions and their asymptotic behaviors at infinite r are

$$|\rho^{(\pm)}_{\mathrm{DQ},\mathcal{N}}\rangle = \sum\!\!\!\!\!\!\int_{\nu} \frac{|R_{\nu,\lambda}\rangle\langle R_{\nu,\lambda}|r\big|R_{n_i,l_i}\big\rangle}{\omega_i + \Omega - \omega_\nu + i0^+} \to -\frac{\pi N_{\kappa_\pm}}{r}\exp[i\Phi_{\kappa_\pm,\lambda}(r)]\langle R_{\kappa_\pm,\lambda}|r\big|R_{n_i,l_i}\big\rangle,$$
$$|\rho^{(\pm)}_{\mathrm{QD},\mathcal{N}}\rangle = \sum\!\!\!\!\!\!\int_{\nu} \frac{|R_{\nu,\lambda}\rangle\langle R_{\nu,\lambda}|r^2\big|R_{n_i,l_i}\big\rangle}{\omega_i + \Omega - \omega_\nu + i0^+} \to -\frac{\pi N_{\kappa_\pm}}{r}\exp[i\Phi_{\kappa_\pm,\lambda}(r)]\langle R_{\kappa_\pm,\lambda}|r^2\big|R_{n_i,l_i}\big\rangle. \tag{D2}$$

Following the asymptotic approximation in Ref. [2] and omitting the fast oscillating term, the integrals $\mathcal{R}^{(\pm)}_{\mathrm{DQ/QD},\mathcal{N}}$ are obtained as

$$\begin{aligned}
\mathcal{R}^{(\pm)}_{\mathrm{QD},\mathcal{N}} =& \langle R_{k,L}|r|\rho^{(\pm)}_{\mathrm{QD},\mathcal{N}}\rangle = -\pi\langle R_{\kappa_\pm,\lambda}|r^2\big|R_{n_i,l_i}\big\rangle\sqrt{\frac{4}{\pi^2\kappa_\pm k}}\int_0^\infty\left[1 - \frac{Z}{2r}\left(\frac{1}{\kappa_\pm^2} + \frac{1}{k^2}\right)\right]\exp(i\Phi_{\kappa_\pm,\lambda})r\sin\Phi_{k,L}dr \\
=& -\pi\langle R_{\kappa_\pm,\lambda}|r^2\big|R_{n_i,l_i}\big\rangle\sqrt{\frac{4}{\pi^2\kappa_\pm k}}\int_0^\infty\exp(i\Phi_{\kappa_\pm,\lambda})r\sin\Phi_{k,L}dr \\
&+ \pi Z\langle R_{\kappa_\pm,\lambda}|r^2\big|R_{n_i,l_i}\big\rangle\left(\frac{1}{\kappa_\pm^2} + \frac{1}{k^2}\right)\sqrt{\frac{4}{\pi^2\kappa_\pm k}}\int_0^\infty\exp(i\Phi_{\kappa_\pm,\lambda})\sin\Phi_{k,L}dr \\
\approx& -\pi\langle R_{\kappa_\pm,\lambda}|r^2\big|R_{n_i,l_i}\big\rangle\sqrt{\frac{1}{\pi^2\kappa_\pm k}}\times\exp\left[-\frac{\pi Z}{2}\left(\frac{1}{\kappa_\pm} - \frac{1}{k}\right)\right]\times\frac{1}{(\kappa_\pm - k)^2} \\
&\times i^{(L-\lambda-1)}\exp[i(\eta_\lambda - \eta_L)]\times\frac{(2\kappa_\pm)^{iZ/\kappa_\pm}}{(2k)^{iZ/k}}\frac{\Gamma\left[2 + iZ\left(\frac{1}{\kappa_\pm} - \frac{1}{k}\right)\right]}{(\kappa_\pm - k)^{iZ(1/\kappa_\pm - 1/k)}}\times\left[1 + \frac{iZ}{2}\left(\frac{1}{\kappa_\pm^2} + \frac{1}{k^2}\right)\frac{\kappa_\pm - k}{1 + iZ(1/\kappa_\pm - 1/k)}\right], \\
\mathcal{R}^{(\pm)}_{\mathrm{DQ},\mathcal{N}} =& \langle R_{k,L}|r^2|\rho^{(\pm)}_{\mathrm{DQ},\mathcal{N}}\rangle = -\pi\langle R_{\kappa_\pm,\lambda}|r|R_{n_i,l_i}\rangle\sqrt{\frac{4}{\pi^2\kappa_\pm k}}\int_0^\infty\left[1 - \frac{Z}{2r}\left(\frac{1}{\kappa_\pm^2} + \frac{1}{k^2}\right)\right]\exp(i\Phi_{\kappa_\pm,\lambda})r^2\sin\Phi_{k,L}dr \\
=& -\pi\langle R_{\kappa_\pm,\lambda}|r\big|R_{n_i,l_i}\big\rangle\sqrt{\frac{4}{\pi^2\kappa_\pm k}}\int_0^\infty\exp(i\Phi_{\kappa_\pm,\lambda})r^2\sin\Phi_{k,L}dr \\
&+ \pi Z\langle R_{\kappa_\pm,\lambda}|r\big|R_{n_i,l_i}\big\rangle\left(\frac{1}{\kappa_\pm^2} + \frac{1}{k^2}\right)\sqrt{\frac{4}{\pi^2\kappa_\pm k}}\int_0^\infty\exp(i\Phi_{\kappa_\pm,\lambda})r\sin\Phi_{k,L}dr \\
\approx& -\pi\langle R_{\kappa_\pm,\lambda}|r\big|R_{n_i,l_i}\big\rangle\sqrt{\frac{1}{\pi^2\kappa_\pm k}}\times\exp\left[-\frac{\pi Z}{2}\left(\frac{1}{\kappa_\pm} - \frac{1}{k}\right)\right] \\
&\times\frac{i^{(L-\lambda)}}{(\kappa_\pm - k)^3}\exp[i(\eta_\lambda - \eta_L)]\times\frac{(2\kappa_\pm)^{iZ/\kappa_\pm}}{(2k)^{iZ/k}}\frac{\Gamma\left[3 + iZ\left(\frac{1}{\kappa_\pm} - \frac{1}{k}\right)\right]}{(\kappa_\pm - k)^{iZ(1/\kappa_\pm - 1/k)}}\times\left[1 + \frac{iZ}{2}\left(\frac{1}{\kappa_\pm^2} + \frac{1}{k^2}\right)\frac{\kappa_\pm - k}{2 + iZ(1/\kappa_\pm - 1/k)}\right],
\end{aligned}$$

with their phases

$$\begin{aligned}
\arg[\mathcal{R}^{(\pm)}_{\mathrm{QD},\mathcal{N}}] &= \frac{\pi}{2}(L - \lambda - 1) + \eta_\lambda(\kappa_\pm) - \eta_L(k) + \phi^{\mathrm{D}}_{\mathrm{cc}}(k,\kappa_\pm), \\
\arg[\mathcal{R}^{(\pm)}_{\mathrm{DQ},\mathcal{N}}] &= \frac{\pi}{2}(L - \lambda) + \eta_\lambda(\kappa_\pm) - \eta_L(k) + \phi^{\mathrm{Q}}_{\mathrm{cc}}(k,\kappa_\pm) + \arg(\kappa_\pm - k).
\end{aligned} \tag{D3}$$

APPENDIX E: THE $2\omega\tau$ MODULATION OF THE FORWARD-BACKWARD ASYMMETRY IN THE SB SIGNALS

With the approximated phases in Eqs. (18), the $2\omega\tau$ oscillations of the forward-backward asymmetry at $\varphi = \varphi_0$ given by Eq. (17), can be written as (except for a factor $1/p$)

$$
\begin{aligned}
\mathcal{I}^{2\omega}_{\rm asy}(E_{2q},\theta,\tau;\varphi_0) &= \mathcal{I}^{2\omega}(E_{2q},\theta,\varphi_0,\tau) - \mathcal{I}^{2\omega}(E_{2q},\theta,\varphi_0+\pi,\tau) \\
&\propto \sum_{L=0,2}\sum_{L'=1,3}\sum_{M'=\pm1} 4\bar{Y}_{L,0}(\theta)\bar{Y}_{L',M'}(\theta)\big\{\big|\mathcal{M}^{(+)}_{\rm DD,L}(E_{2q})\big|\big|\mathcal{M}^{(-)}_{\rm DQ,L'}(E_{2q})\big|\cos[2\omega\tau+\phi^{(+)}_{{\rm DD},\lambda}(E_{2q}) \\
&\quad -\phi^{(-)}_{{\rm DQ},\lambda}(E_{2q}) - M'\varphi_0] + |\mathcal{M}^{(-)}_{\rm DD,L}(E_{2q})||\mathcal{M}^{(+)}_{\rm DQ,L'}(E_{2q})|\cos[2\omega\tau-\phi^{(-)}_{{\rm DD},\lambda}(E_{2q})+\phi^{(+)}_{{\rm DQ},\lambda}(E_{2q}) \\
&\quad +M'\varphi_0] + |\mathcal{M}^{(+)}_{\rm DD,L}(E_{2q})||\mathcal{M}^{(-)}_{\rm QD,L'}(E_{2q})|\cos[2\omega\tau+\phi^{(+)}_{{\rm DD},\lambda}(E_{2q})-\phi^{(-)}_{{\rm QD},\lambda}(E_{2q})-M'\varphi_0] \\
&\quad +|\mathcal{M}^{(-)}_{\rm DD,L}(E_{2q})||\mathcal{M}^{(+)}_{\rm QD,L'}(E_{2q})|\cos[2\omega\tau-\phi^{(-)}_{{\rm DD},\lambda}(E_{2q})+\phi^{(+)}_{{\rm QD},\lambda}(E_{2q})+M'\varphi_0] \\
&= \sum_{L=0,2}\sum_{L'=1,3} 8\sin\varphi_0\bar{Y}_{L,0}(\theta)\bar{Y}_{L',1}(\theta)\big\{|\mathcal{M}^{(+)}_{\rm DD,L}(E_{2q})||\mathcal{M}^{(-)}_{\rm DQ,L'}(E_{2q})|\sin[2\omega\tau+\phi^{(+)}_{{\rm DD},\lambda}(E_{2q}) \\
&\quad -\phi^{(-)}_{{\rm DQ},\lambda}(E_{2q})] - |\mathcal{M}^{(-)}_{\rm DD,L}(E_{2q})||\mathcal{M}^{(+)}_{\rm DQ,L'}(E_{2q})|\sin[2\omega\tau-\phi^{(-)}_{{\rm DD},\lambda}(E_{2q})+\phi^{(+)}_{{\rm DQ},\lambda}(E_{2q})] \\
&\quad + |\mathcal{M}^{(+)}_{\rm DD,L}(E_{2q})||\mathcal{M}^{(-)}_{\rm QD,L'}(E_{2q})|\sin[2\omega\tau+\phi^{(+)}_{{\rm DD},\lambda}(E_{2q})-\phi^{(-)}_{{\rm QD},\lambda}(E_{2q})] \\
&\quad - |\mathcal{M}^{(-)}_{\rm DD,L}(E_{2q})||\mathcal{M}^{(+)}_{\rm QD,L'}(E_{2q})|\sin[2\omega\tau-\phi^{(-)}_{{\rm DD},\lambda}(E_{2q})+\phi^{(+)}_{{\rm QD},\lambda}(E_{2q})]\big\} \\
&= \sum_{L=0,2}\sum_{L'=1,3} 8\sin\varphi_0\bar{Y}_{L,0}(\theta)\bar{Y}_{L',1}(\theta)\big\{\big|\mathcal{M}^{(+)}_{\rm DD,L}(E_{2q})\big|\big|\mathcal{M}^{(-)}_{\rm DQ,L'}(E_{2q})\big| \\
&\quad \times \sin\Big[2\omega\tau+\eta_{\lambda=1}(\kappa_+)+\phi^{\rm D}_{\rm cc}(k,\kappa_+)-\eta_{\lambda=1}(\kappa_-)-\phi^{\rm Q}_{\rm cc}(k,\kappa_-)-\frac{\pi}{2}\Big] \\
&\quad -\big|\mathcal{M}^{(-)}_{\rm DD,L}(E_{2q})\big|\big|\mathcal{M}^{(+)}_{\rm DQ,L'}(E_{2q})\big|\sin\Big[2\omega\tau-\eta_{\lambda=1}(\kappa_-)-\phi^{\rm D}_{\rm cc}(k,\kappa_-)+\eta_{\lambda=1}(\kappa_+)+\phi^{\rm Q}_{\rm cc}(k,\kappa_+)+\frac{\pi}{2}\Big] \\
&\quad + \big|\mathcal{M}^{(+)}_{\rm DD,L}(E_{2q})\big|\big|\mathcal{M}^{(-)}_{\rm QD,L'}(E_{2q})\big|\sin\Big[2\omega\tau+\eta_{\lambda=1}(\kappa_+)+\phi^{\rm D}_{\rm cc}(k,\kappa_+)-\eta_{\lambda=2}(\kappa_-)-\phi^{\rm D}_{\rm cc}(k,\kappa_-)-\frac{\pi}{2}\Big] \\
&\quad - \big|\mathcal{M}^{(-)}_{\rm DD,L}(E_{2q})\big|\big|\mathcal{M}^{(+)}_{\rm QD,L'}(E_{2q})\big|\sin\Big[2\omega\tau-\eta_{\lambda=1}(\kappa_-)-\phi^{\rm D}_{\rm cc}(k,\kappa_-)+\eta_{\lambda=2}(\kappa_+)+\phi^{\rm D}_{\rm cc}(k,\kappa_+)+\frac{\pi}{2}\Big]\Big\} \\
&= \sum_{L=0,2}\sum_{L'=1,3} -8\sin\varphi_0\bar{Y}_{L,0}(\theta)\bar{Y}_{L',1}(\theta)\big\{\big|\mathcal{M}^{(+)}_{\rm DD,L}(E_{2q})\big|\big|\mathcal{M}^{(-)}_{\rm DQ,L'}(E_{2q})\big| \\
&\quad \times \cos\big[2\omega\tau+\eta_{\lambda=1}(\kappa_+)+\phi^{\rm D}_{\rm cc}(k,\kappa_+)-\eta_{\lambda=1}(\kappa_-)-\phi^{\rm Q}_{\rm cc}(k,\kappa_-)\big] \\
&\quad +|\mathcal{M}^{(-)}_{\rm DD,L}(E_{2q})||\mathcal{M}^{(+)}_{\rm DQ,L'}(E_{2q})|\cos\big[2\omega\tau-\eta_{\lambda=1}(\kappa_-)-\phi^{\rm D}_{\rm cc}(k,\kappa_-)+\eta_{\lambda=1}(\kappa_+)+\phi^{\rm Q}_{\rm cc}(k,\kappa_+)\big] \\
&\quad + |\mathcal{M}^{(+)}_{\rm DD,L}(E_{2q})||\mathcal{M}^{(-)}_{\rm QD,L'}(E_{2q})|\cos\big[2\omega\tau+\eta_{\lambda=1}(\kappa_+)+\phi^{\rm D}_{\rm cc}(k,\kappa_+)-\eta_{\lambda=2}(\kappa_-)-\phi^{\rm D}_{\rm cc}(k,\kappa_-)\big] \\
&\quad + |\mathcal{M}^{(-)}_{\rm DD,L}(E_{2q})||\mathcal{M}^{(+)}_{\rm QD,L'}(E_{2q})|\cos\big[2\omega\tau-\eta_{\lambda=1}(\kappa_-)-\phi^{\rm D}_{\rm cc}(k,\kappa_-)+\eta_{\lambda=2}(\kappa_+)+\phi^{\rm D}_{\rm cc}(k,\kappa_+)\big]\big\}.
\end{aligned}
$$

Here the relation $\bar{Y}_{l,-m}(\theta) = (-1)^m\bar{Y}_{l,m}(\theta)$ is used, where $Y_{l,m}(\theta,\varphi) = \bar{Y}_{l,m}(\theta)e^{im\varphi}$ and $\bar{Y}_{l,m}(\theta) = (-1)^m\sqrt{\frac{2l+1}{4\pi}\frac{(l-m)!}{(l+m)!}}P^m_l(\cos\theta)$, with $P^m_l(\cos\theta)$ the associated Legendre polynomial.

[1] R. Pazourek, S. Nagele, and J. Burgdörfer, Rev. Mod. Phys. **87**, 765 (2015).

[2] J. M. Dahlström, A. L'Huillier, and A. Maquet, J. Phys. B **45**, 183001 (2012).

[3] J. Dahlström, D. Guénot, K. Klünder, M. Gisselbrecht, J. Mauritsson, A. L'Huillier, A. Maquet, and R. Taïeb, Chem. Phys. **414**, 53 (2013), Attosecond spectroscopy.

[4] M. Hentschel, R. Kienberger, C. Spielmann, G. A. Reider, N. Milosevic, T. Brabec, P. Corkum, U. Heinzmann, M. Drescher, and F. Krausz, Nature (London) **414**, 509 (2001).

[5] P. M. Paul, E. S. Toma, P. Breger, G. Mullot, F. Augé, P. Balcou, H. G. Muller, and P. Agostini, Science **292**, 1689 (2001).

[6] M. Isinger, R. J. Squibb, D. Busto, S. Zhong, A. Harth, D. Kroon, S. Nandi, C. L. Arnold, M. Miranda, J. M. Dahlström, E. Lindroth, R. Feifel, M. Gisselbrecht, and A. L'Huillier, Science **358**, 893 (2017).

[7] S. Beaulieu, A. Comby, A. Clergerie, J. Caillat, D. Descamps, N. Dudovich, B. Fabre, R. Géneaux, F. Légaré, S. Petit, B. Pons, G. Porat, T. Ruchon, R. Taïeb, V. Blanchet, and Y. Mairesse, Science **358**, 1288 (2017).

[8] M. Lucchini, L. Castiglioni, L. Kasmi, P. Kliuiev, A. Ludwig, M. Greif, J. Osterwalder, M. Hengsberger, L. Gallmann, and U. Keller, Phys. Rev. Lett. **115**, 137401 (2015).

[9] I. Jordan, M. Huppert, D. Rattenbacher, M. Peper, D. Jelovina, C. Perry, A. von Conta, A. Schild, and H. J. Wörner, Science **369**, 974 (2020).

[10] E. S. Toma and H. G. Muller, J. Phys. B **35**, 3435 (2002).

[11] V. Véniard, R. Taïeb, and A. Maquet, Phys. Rev. A **54**, 721 (1996).

[12] R. Géneaux, A. Camper, T. Auguste, O. Gobert, J. Caillat, R. Taïeb, and T. Ruchon, Nat. Commun. **7**, 12583 (2016).

[13] V. Gruson, L. Barreau, Á. Jiménez-Galan, F. Risoud, J. Caillat, A. Maquet, B. Carré, F. Lepetit, J.-F. Hergott, T. Ruchon, L. Argenti, R. Taïeb, F. Martín, and P. Salières, Science **354**, 734 (2016).

[14] S. Zhong, J. Vinbladh, D. Busto, R. J. Squibb, M. Isinger, L. Neoričić, H. Laurell, R. Weissenbilder, C. L. Arnold, R. Feifel, J. M. Dahlström, G. Wendin, M. Gisselbrecht, E. Lindroth, and A. L'Huillier, Nat. Commun. **11**, 5042 (2020).

[15] S. Biswas, B. Förg, L. Ortmann, J. Schötz, W. Schweinberger, T. Zimmermann, L. Pi, D. Baykusheva, H. A. Masood, I. Liontos, A. M. Kamal, N. G. Kling, A. F. Alharbi, M. Alharbi, A. M. Azzeer, G. Hartmann, H. J. Wörner, A. S. Landsman, and M. F. Kling, Nat. Phys. **16**, 778 (2020).

[16] X. Gong, W. Jiang, J. Tong, J. Qiang, P. Lu, H. Ni, R. Lucchese, K. Ueda, and J. Wu, Phys. Rev. X **12**, 011002 (2022).

[17] A. Jiménez-Galán, F. Martín, and L. Argenti, Phys. Rev. A **93**, 023429 (2016).

[18] K. Klünder, J. M. Dahlström, M. Gisselbrecht, T. Fordell, M. Swoboda, D. Guénot, P. Johnsson, J. Caillat, J. Mauritsson, A. Maquet, R. Taïeb, and A. L'Huillier, Phys. Rev. Lett. **106**, 143002 (2011).

[19] O. Hemmers, R. Guillemin, and D. W. Lindle, Radiat. Phys. Chem. **70**, 123 (2004), Photoeffect: theory and experiment.

[20] L. Argenti and R. Moccia, J. Phys. B **43**, 235006 (2010).

[21] R. Guillemin, O. Hemmers, D. W. Lindle, and S. T. Manson, Radiat. Phys. Chem. **75**, 2258 (2006), New directions in the study of interaction of energetic photons with matter.

[22] M. O. Krause, Phys. Rev. **177**, 151 (1969).

[23] J. W. Cooper, Phys. Rev. A **47**, 1841 (1993).

[24] S. Grundmann, M. Kircher, I. Vela-Perez, G. Nalin, D. Trabert, N. Anders, N. Melzer, J. Rist, A. Pier, N. Strenger, J. Siebert, P. V. Demekhin, L. P. H. Schmidt, F. Trinter, M. S. Schöffler, T. Jahnke, and R. Dörner, Phys. Rev. Lett. **124**, 233201 (2020).

[25] S. Grundmann, D. Trabert, K. Fehre, N. Strenger, A. Pier, L. Kaiser, M. Kircher, M. Weller, S. Eckart, L. P. H. Schmidt, F. Trinter, T. Jahnke, M. S. Schöffler, and R. Dörner, Science **370**, 339 (2020).

[26] M. Y. Amusia and L. V. Chernysheva, JETP Lett. **112**, 673 (2020).

[27] G. B. Pradhan, J. Jose, P. C. Deshmukh, L. A. LaJohn, R. H. Pratt, and S. T. Manson, J. Phys. B **44**, 201001 (2011).

[28] M. Ilchen, G. Hartmann, E. V. Gryzlova, A. Achner, E. Allaria, A. Beckmann, M. Braune, J. Buck, C. Callegari, R. N. Coffee, R. Cucini, M. Danailov, A. De Fanis, A. Demidovich, E. Ferrari, P. Finetti, L. Glaser, A. Knie, A. O. Lindahl, O. Plekan *et al.*, Nat. Commun. **9**, 4659 (2018).

[29] N. L. S. Martin, D. B. Thompson, R. P. Bauman, C. D. Caldwell, M. O. Krause, S. P. Frigo, and M. Wilson, Phys. Rev. Lett. **81**, 1199 (1998).

[30] V. K. Dolmatov and S. T. Manson, Phys. Rev. Lett. **83**, 939 (1999).

[31] P. Lambropoulos, G. Doolen, and S. P. Rountree, Phys. Rev. Lett. **34**, 636 (1975).

[32] M. Lambropoulos, S. E. Moody, S. J. Smith, and W. C. Lineberger, Phys. Rev. Lett. **35**, 159 (1975).

[33] J. Maurer and U. Keller, J. Phys. B **54**, 094001 (2021).

[34] H. R. Reiss, Phys. Rev. Lett. **101**, 043002 (2008).

[35] E. Stambulchik and Y. Maron, Phys. Rev. Lett. **113**, 083002 (2014).

[36] C. T. L. Smeenk, L. Arissian, B. Zhou, A. Mysyrowicz, D. M. Villeneuve, A. Staudte, and P. B. Corkum, Phys. Rev. Lett. **106**, 193002 (2011).

[37] H. Ni, S. Brennecke, X. Gao, P.-L. He, S. Donsa, I. Březinová, F. He, J. Wu, M. Lein, X.-M. Tong, and J. Burgdörfer, Phys. Rev. Lett. **125**, 073202 (2020).

[38] M. Klaiber, E. Yakaboylu, H. Bauke, K. Z. Hatsagortsyan, and C. H. Keitel, Phys. Rev. Lett. **110**, 153004 (2013).

[39] S. Chelkowski, A. D. Bandrauk, and P. B. Corkum, Phys. Rev. Lett. **113**, 263005 (2014).

[40] P.-L. He, D. Lao, and F. He, Phys. Rev. Lett. **118**, 163203 (2017).

[41] A. Ludwig, J. Maurer, B. W. Mayer, C. R. Phillips, L. Gallmann, and U. Keller, Phys. Rev. Lett. **113**, 243001 (2014).

[42] N. Haram, I. Ivanov, H. Xu, K. T. Kim, A. Atia-tul-Noor, U. S. Sainadh, R. D. Glover, D. Chetty, I. V. Litvinyuk, and R. T. Sang, Phys. Rev. Lett. **123**, 093201 (2019).

[43] A. Hartung, S. Brennecke, K. Lin, D. Trabert, K. Fehre, J. Rist, M. S. Schöffler, T. Jahnke, L. P. H. Schmidt, M. Kunitski, M. Lein, R. Dörner, and S. Eckart, Phys. Rev. Lett. **126**, 053202 (2021).

[44] M. Førre, S. Selstø, J. P. Hansen, and L. B. Madsen, Phys. Rev. Lett. **95**, 043601 (2005).

[45] J. Liang, M. Han, Y. Liao, J.-b. Ji, C. S. Leung, W.-C. Jiang, K. Ueda, Y. Zhou, P. Lu, and H. J. Wörner, Nat. Photon. **18**, 311 (2024).

[46] A. N. Grum-Grzhimailo and E. V. Gryzlova, Phys. Rev. A **89**, 043424 (2014).

[47] A. Bechler and R. H. Pratt, Phys. Rev. A **39**, 1774 (1989).

[48] H. R. Varma, M. F. Ciappina, N. Rohringer, and R. Santra, Phys. Rev. A **80**, 053424 (2009).

[49] V. Florescu, O. Budriga, and H. Bachau, Phys. Rev. A **84**, 033425 (2011).

[50] M. Dondera and H. Bachau, Phys. Rev. A **85**, 013423 (2012).

[51] V. Florescu, O. Budriga, and H. Bachau, Phys. Rev. A **86**, 033413 (2012).

[52] C. J. Joachain, N. J. Kylstra, and R. M. Potvliege, *Atoms in Intense Laser Fields* (Cambridge University Press, Cambridge, 2011).

[53] H. G. Muller, Phys. Rev. A **60**, 1341 (1999).

[54] A. Hartung, S. Eckart, S. Brennecke, J. Rist, D. Trabert, K. Fehre, M. Richter, H. Sann, S. Zeller, K. Henrichs, G. Kastirke, J. Hoehl, A. Kalinin, M. S. Schöffler, T. Jahnke, L. P. H. Schmidt, M. Lein, M. Kunitski, and R. Dörner, Nat. Phys. **15**, 1222 (2019).

[55] S. Brennecke and M. Lein, J. Phys. B **51**, 094005 (2018).

[56] M. Førre and A. S. Simonsen, Phys. Rev. A **93**, 013423 (2016).

[57] M. Førre and S. Selstø, Phys. Rev. A **101**, 063416 (2020).

[58] J. Liang, W. Wang, K. Liu, W.-C. Jiang, L. Guo, Y. Zhou, and P. Lu, Phys. Rev. A **109**, 023102 (2024).

[59] T. K. Lindblom, M. Førre, E. Lindroth, and S. Selstø, Phys. Rev. Lett. **121**, 253202 (2018).
[60] A. S. Kheifets, Phys. Rev. A **104**, L021103 (2021).
[61] T. N. Rescigno and C. W. McCurdy, Phys. Rev. A **62**, 032706 (2000).
[62] W.-C. Jiang and X.-Q. Tian, Opt. Express **25**, 26832 (2017).
[63] J. Liang, Y. Zhou, Y. Liao, W.-C. Jiang, M. Li, and P. Lu, Ultrafast Sci. **2022**, 9842716 (2022).
[64] D. G. Arbó, J. E. Miraglia, M. S. Gravielle, K. Schiessl, E. Persson, and J. Burgdörfer, Phys. Rev. A **77**, 013401 (2008).
[65] S. Brennecke and M. Lein, Phys. Rev. A **104**, L021104 (2021).
[66] N. J. Kylstra, R. M. Potvliege, and C. J. Joachain, J. Phys. B **34**, L55 (2001).
[67] E. A. Power and T. Thirunamachandran, Proc. R. Soc. A **372**, 265 (1980).
[68] E. A. Power, S. Zienau, and H. S. W. Massey, Philos. Trans. R. Soc. London, Ser. A **251**, 427 (1959).
[69] R. G. Woolley and C. A. Coulson, Proc. R. Soc. London, Ser. A **321**, 557 (1971).
[70] R. G. Woolley, J. Phys. A **13**, 2795 (1980).
[71] D. H. Kobe, Am. J. Phys. **49**, 581 (1981).
[72] R. Loudon, *The Quantum Theory of Light* (Oxford University Press, Oxford, 2000).
[73] A. Bonvicini and B. Champagne, J. Chem. Phys. **159**, 114107 (2023).
[74] W. P. Healy, J. Chem. Phys. **64**, 3111 (1976).
[75] M. Y. Amusia and L. V. Chernysheva, Angular distribution of photoelectrons and secondary electrons outside the dipole approximation, in *Computation of Atomic and Molecular Processes: Introducing the ATOM-M Software Suite* (Springer International, Cham, 2021), pp. 199–219.
[76] E. A. Power and T. Thirunamachandran, J. Phys. B **8**, L170 (1975).
[77] M. Babiker and R. Loudon, Proc. R. Soc. A **385**, 439 (1983).
[78] Y. Liao, E. Olofsson, J. M. Dahlström, L.-W. Pi, Y. Zhou, and P. Lu, Phys. Rev. A **109**, 043104 (2024).
[79] Á. Jiménez Galán, L. Argenti, and F. Martín, New J. Phys. **15**, 113009 (2013).
[80] D. Busto, J. Vinbladh, S. Zhong, M. Isinger, S. Nandi, S. Maclot, P. Johnsson, M. Gisselbrecht, A. L'Huillier, E. Lindroth, and J. M. Dahlström, Phys. Rev. Lett. **123**, 133201 (2019).
[81] M. Bertolino, D. Busto, F. Zapata, and J. M. Dahlström, J. Phys. B **53**, 144002 (2020).
[82] A. F. Starace, Theory of Atomic Photoionization, Handbuch Phys. **31**, 1 (1982).
[83] A. Dalgarno, J. T. Lewis, and D. R. Bates, Proc. R. Soc. A **233**, 70 (1955).
[84] L.-W. Pi and A. F. Starace, Phys. Rev. A **90**, 023403 (2014).
[85] M. Aymar and M. Crance, J. Phys. B **14**, 3585 (1981).
[86] B. Gao and A. F. Starace, Comput. Phys. **1**, 70 (1987).
[87] D. V. Rezvan, K. Klyssek, S. Grundmann, A. Pier, N. M. Novikovskiy, N. Strenger, D. Tsitsonis, M. Kircher, I. Vela-Peréz, K. Fehre, F. Trinter, M. S. Schöffler, T. Jahnke, R. Dörner, and P. V. Demekhin, Phys. Rev. Lett. **129**, 253201 (2022).
[88] A. Bechler and R. H. Pratt, Phys. Rev. A **42**, 6400 (1990).
[89] X. Mu and B. Crasemann, Phys. Rev. A **38**, 4585 (1988).
[90] C. Cohen-Tannoudji, J. Dupont-Roc, and G. Grynberg, *Atom-Photon Interactions: Basic Processes and Applications* (Wiley, 1998).